Erosion around a large-scale topographic high in a semi-arid sedimentary basin: Interactions between fluvial erosion, aeolian erosion and aeolian transport

Marc Jolivet, Regis Braucher, D. Dovchintseren, S. Hocquet, J.-M. Schmitt

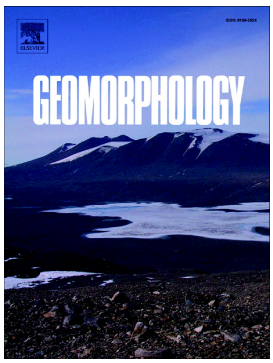

Erosion around a large-scale topographic high in a semi-arid sedimentary basin: Interactions between fluvial erosion, aeolian erosion and aeolian transport

M. Jolivet, R. Braucher, D. Dovchintseren, S. Hocquet, J.-M. Schmitt, ASTER Team

PII: S0169-555X(21)00155-0

DOI: https://doi.org/10.1016/j.geomorph.2021.107747

Reference: GEOMOR 107747

To appear in: *Geomorphology*

Received date: 8 January 2021

Revised date: 1 April 2021

Accepted date: 12 April 2021

Please cite this article as: M. Jolivet, R. Braucher, D. Dovchintseren, et al., Erosion around a large-scale topographic high in a semi-arid sedimentary basin: Interactions between fluvial erosion, aeolian erosion and aeolian transport, *Geomorphology* (2021), https://doi.org/10.1016/j.geomorph.2021.107747

Erosion around a large-scale topographic high in a semi-arid sedimentary basin: Interactions between fluvial erosion, aeolian erosion and aeolian transport.

M. Jolivet[a,*], R. Braucher[b], D. Dovchintseren[a,c], S. Hocquet[b], J-M., Schmitt[b], ASTER Team[+,b]

[a] Univ Rennes, CNRS, Géosciences Rennes, UMR6118, CNRS – F-35000 Rennes, France

[b] Aix-Marseille Univ, CNRS-IRD-Collège de France-INRAE, UMR34 CEREGE, Technopôle de l'Environnement Arbois et Méditerranée, BP80 13545 Aix-en-Provence, France

[c] Orano Mining, 1, place J. Millier, 92400 Courbevois, France

+ ASTER Team: G. Aumaître, D. Bourlès, K. Keddadouche.

Abstract

Large-scale aeolian erosion features such as pans usually develop upon a relatively homogeneous erodible sedimentary rock substratum and show simple concave morphologies. However, some erosional depressions in semi-arid to arid settings develop in more complex geological contexts, associating sedimentary basins and outcrops of non-erodible basement. In semi-arid basins, the geomorphic evolution is controlled by interplay between the processes of fluvial erosion and deposition (especially of the finer sediment fraction in ephemeral lakes) and the processes of aeolian erosion and deflation. The occurrence of non-erodible basement outcrops within a region of overall deflation complicates drainage systems and wind-flow patterns. Both are liable to evolve rapidly through time and their interactions remain poorly understood. In this study, we use a detailed geomorphological analysis, including mapping of the aeolian sand-motion direction within the 16,300 km^2 Tsagaan Els depression (Gobi Desert, Mongolia) as well as in situ-produced cosmogenic ^{10}Be and ^{26}Al based quantitative constraints, to propose a conceptual model for the morphologic evolution of geologically complex semi-arid basins. Based on theoretical studies of wind-flow patterns around obstacles, we demonstrate that the occurrence of erosion-resistant basement highs inside the basin induces the localization of preferential deflation zones and aeolian and fluvial carving of large-scale relief. The enhanced deflation zones form sub-depocenters controlling local drainage systems that mobilize clastic material and transport it to the deflation zone. These river systems are frequently captured by neighboring streams, which creates unstable conditions of erosion and deposition. Such rapid modifications of the topography through time affect the hydrogeologic structure of the basin and may impact potential sediment-hosted mineral deposits.

Keywords

Aeolian erosion; Fluvial-aeolian interaction; Aeolian geomorphology; Cosmogenic radionuclides; Gobi desert

1. Introduction

Aeolian erosion generates a number of geomorphic structures whose sizes span from centimeter scale ventifacts to meter- to tens of kilometers-scale yardangs, and to blowouts and pans that can be hundreds of kilometers in diameter (Blackwelder, 1934; Goudie, 1989; Goudie and Wells, 1995; Hesp, 2002; Laity, 2011). Pans form relatively flat, closed depressions that may cover thousands of square kilometers, such as the Etosha pan in Namibia (Hipondoka, 2005; Miller et al., 2010). Those that do not have a karstic origin (Albritton et al., 1990) usually form upon sedimentary rocks in wide flat areas mostly through a combination of wind deflation, salt weathering and, during wetter periods, lacustrine processes (waves) (Goudie, 1991; Wormald et al., 2003). In the absence of erosion-resistant obstacles, pans have a rounded to oval shape due to the relatively homogeneous mechanical resistance to erosion of the substratum (Goudie, 1991; Goudie and Wells, 1995). Indeed, wind erosion associates deflation (removal of loose particles by the wind) and wind abrasion (removal of attached particles through impacts of transported grains). Unless the substratum is poorly consolidated, the initial mobilization of particles is generally caused by fluvial erosion or weathering. Wind abrasion (hereafter referred as abrasion) is generally only bringing a minor contribution to the material available to wind-transport (Aref et al., 2002; Laity, 2011). Deflation and abrasion are mainly controlled by the wind velocity (Bagnold, 1941; Iversen et al., 1990). In flat, obstacle-free regions, the wind velocity and direction can be considered as constant over the whole surface, leading to the rounded form of large blowouts or pans that can develop from an initial surface disturbance such as fault scarps, river channels or dry lakes (Goudie, 1991; Wormald et al., 2003; Barchyn and Hugenholtz, 2013). When obstacles are present, the wind flow becomes more complex as eddies, reversed flow regions, wind-acceleration zones and wind channels start to develop (Hunt et al., 1978; Laity, 1987; Ruszkiczay-Rüdiger et al., 2007, 2009, 2011; Sebe et al., 2011). This in turns leads to the localization of preferential erosion and sand deposition zones, increasing the complexity of the topography.

Using analog (Castro and Robins, 1977; Hunt et al., 1978; Iversen et al., 1990; Tominaga et al., 2018) and numerical modeling (Badr and Harion, 2005, 2007; Wakes et al., 2010; Jackson et al., 2013; Tominaga et al., 2018; Liu et al., 2019), numerous studies have addressed the effects of obstacles or topography on the wind flow pattern. These studies mainly addressed the localization of preferential deflation zones or wind shadows. However, although in many natural dryland settings, fluvial processes interact with the aeolian sediment-transport and erosion processes, these studies only deal with wind dynamics and never take into account the role of fluvial erosion in creating loose particles, transporting them outside or inside the system or segregating them by size. Furthermore, when applied to natural cases, many of these studies deal with simple, small-scale topographies such as dune fields or small hills. Another series of studies based on satellite images and completely disconnected from the fluid dynamics approach, describe the interactions between aeolian dunes and large rivers (Krapf et al., 2003; Liu and Coulthard, 2015, 2017; Al-Masrahy and Mountney, 2015), investigate the role of fine-grained river deposits in providing material to dune fields (Maroulis et al., 2007) or, on the contrary the reworking of fine-grained aeolian loess deposits by rivers (Williams, 2015). However, these studies do not consider the erosion mechanism at the source of the detrital material and little quantitative information is provided (erosion or sedimentation rates). Finally, several field-based studies have addressed the exchange of sediment particles between fluvial and aeolian systems depending on the sediment availability in rivers or dunes and the vegetation cover (Mush et al., 1996; Bullard and Livingstone, 2002; Draut, 2012; Sankey et al., 2018a) or river flow (Sankey et al., 2018b; Santos et al., 2019).

A key question that therefore remains is how to most effectively quantify how fluvial and aeolian processes interact in driving the long-term topographic expression of large-scale obstacles. We will address this question through a geomorphological study of a series of small basins separated by basement highs in the Gobi desert of Mongolia. The endoreic setting of this region prevents changes in boundary conditions to the studied system, especially the capture and generally associated rapid modification of the fluvial system by an adjacent drainage area. Furthermore, the Gobi Desert has an arid climate with intense aeolian activity and vegetation is limited to grass and small saxaul bushes (*Haloxylon* sp.). Such a setting, including a complex drainage system, active aeolian processes, the near absence of vegetation and a marked lithological substratum pattern, is ideal to study the interaction between aeolian and fluvial processes. The aim of the work described below is to propose a conceptual model of landscape evolution resulting from aeolian and fluvial interactions around a large natural obstacle within a sedimentary basin.

2. Description of the study area and methodology

A first estimate of the wind pattern over the study area was obtained using the European Centre for Medium-Range Weather Forecast Re-Analysis (ERA-Interim) model that provides 10 m above ground wind velocity and direction data. In order to investigate the interplay between fluvial erosion and deflation, we mapped the drainage network with special focus on positioning local base levels. We then mapped the sand-transport directions as reflecting the wind-flow pattern at ground level and correlated this pattern with the surface morphology (including the drainage system) to detect potential preferential deflation zones. We also measured in situ-produced concentrations of the ^{10}Be and ^{26}Al cosmogenic nuclides to quantify the erosion rates over the basin and to better understand the effect of the basement highs on the large-scale erosion pattern.

2.1. Geomorphology and hydrology of the Tsagaan Els depression

The Tsagaan Els depression in SE Mongolia is a ~16,300 km^2 endorheic depression subdivided by the North Zuunbayan fault zone into the Unegt sub-basin to the north and the Zuunbayan sub-basin to the south (Figure 1) (Graham et al., 2001; Grizzard et al., 2019). The entire depression is undergoing active erosion and surface lowering. The lowest point of the depression is 700 m above sea level (a.s.l.) and is situated within the eastern part of the Zuunbayan sub-basin with a second low zone (750 m a.s.l.) in the SW part of the Unegt sub-basin (Figure 1). The basin floor consists of sedimentary bedrock covered by a thin layer of gravel pavement and aeolian dunes in some places (see description below). The complex drainage system of the depression is composed of a fractal-like series of sub-systems associated with local base levels filled by ephemeral lakes in which water is only present for very short periods of time, generally following heavy rain events. This includes the effective base level of the depression situated in the NE part of the Zuunbayan sub-basin that forms a large playa (Figure 1). Some of those sub-systems are associated with large rivers, all of which are ephemeral or seasonal (no baseflow), due to the arid climate but many are formed by a series of small, poorly organized drains showing sharp knickpoints implying rapid incision due to base-level drop (Whipple and Tucker, 1999; Crosby and Whipple, 2006). The present-day Tsagaan Els depression is superimposed on a complex pattern of Upper Jurassic – Lower Cretaceous grabens and half-grabens sealed by Late Cretaceous to Cenozoic post-rift alluvial, lacustrine and aeolian deposits including carbonate paleosols (Johnson et al., 2001; Graham et al., 2001; Johnson, 2004; Webb and Johnson, 2006; Daoudene et al., 2017). Thin Paleogene to Neogene strata contain numerous aeolian dune deposits and calcisols, both indicating a long-lasting arid to semi-arid

climate (Currie and Eberth, 1993; Caves et al., 2014; Naugolnykh, 2016). The Mesozoic basins are separated by or contain fault-limited basement highs composed of Proterozoic to Paleozoic crystalline rocks (Webb and Johnson, 2006; Daoudene et al., 2017).

In the center of the Tsagaan Els depression, the c.a. 55 km long, 20 km wide Tavan Har basement high culminates around 975 m a.s.l. and 250 m above the lowest point of the depression (Figures 2 and 3a). Similarly, to all the exposed basement highs in the Tsagaan Els region, the Tavan Har hill is characterized by a flat summit corresponding to a regional erosional planation paleosurface (Figure 3a and d) (Jolivet et al., 2007; Vassallo et al., 2007). Large areas of the plateau are devoid of sediments, except for some Quaternary sand sheets, some of them filling small canyons (Figure 3d). On the slopes that are not covered by Mesozoic sediments, colluvial forms a few centimeter- to decimeter-thick layer of sharp edged, unsorted, in-situ produced basement blocks and gravels mixed with aeolian sand.

The northern edge of the Tavan Har horst is limited by the NE-SW striking North Zuunbayan fault zone (Figure 3b). Cretaceous strata are exposed along the northern margin of the Tavan Har hill, with bedding largely sequent to the surface morphology (Figure 3b), itself characterized by a north-facing conical structure linking the summit of the basement high to the lowest part of the Unegt sub-basin (Figures 2 and 3b). This structure eroded into the Cretaceous series corresponds to a bedrock pediment supporting active meter-high aeolian dunes, decimeter-thick sand sheets and centimeter-thick layers of strongly wind-polished gravels originating from the underlying Cretaceous deposits (Figure 3e and Supplementary Figure 1). The present-day depocenter of the Unegt sub-basin is occupied by a series of ephemeral lakes (Belnap and Ludwig, 2001) distributed along an arcuate line parallel to the front of the Tavan Har conical structure (Figure 2). To the north, the topography rises again up to the summit of the Mandakh-Saykhanduklaan basement ridge which limits the northern part of the Tsagaan Els depression (Figure 1).

To the south, the Tavan Har basement high is limited by a series of NE-SW striking Early Cretaceous normal faults (Figures 2 and 3c). The relief between the metamorphic basement and the Zuunbayan sub-basin is generally steep, corresponding to differential erosion of the fault planes. Although the depocenter of the Zuunbayan sub-basin is situated some 35 km NE of the eastern reach of the Tavan Har hill, two secondary depressions form local depocenters immediately NE and SW of the basement high (Figures 1 and 2). The NE depression is largely elliptical, with a lowest point at 760 m, about 150 m below the mean altitude of the eastern part of the Tavan Har plateau. The bottom of the depression corresponds to an ephemeral lake. The drainage system associated with the depression is mainly composed of two rivers, one flowing from the SW along the edge of

the Tavan Har basement high, the other coming from the south with a source in the Totoshan basement ridge (Figure 2). This closed depression contains the only exposure of lower Cretaceous strata in the western part of the Zuunbayan sub-basin. The SW depression is elliptical, with a long axis parallel to the edge of the basement high. The lowest part of the depression is again formed by an ephemeral lake at an altitude of 760 m. However, unlike in the NE depression, only Late Cretaceous strata are exposed, suggesting a lower amount of denudation. The drainage system associated with the depression is formed by a single river flowing from the southern part of the Tavan Har basement high (Figure 2).

The Tsagaan Els depression contains several active dune fields (Figures 4 and 5). They range in size from 100 to 1000 km^2, contain meter- to decameter-thick accumulations of sand and show well developed parabolic and transverse dunes (Figure 5a). Others are only sand sheets of a few centimeters to decimeters thick with few parabolic dunes. Some of the dune fields are geographically closely associated with water saturated areas such as ephemeral lakes, major rivers or springs (Mountney and Russell, 2009). For both parabolic and transverse dunes, the crest lines are sub-perpendicular to the sand-transport direction (Mountney, 2006; Courrech du Pont et al., 2014; Gao et al., 2015). In some specific places such as downwind of ephemeral lakes that provide fine-grained unconsolidated material, raked linear dunes are present with their long axis parallel to the sand transport direction (Figure 5b) (Mountney, 2006; Courrech du Pont et al., 2014). However, most of the depression is characterized by a lag deposit forming a reg-type ground (the term reg refers to a rocky desert with a limited amount of sand) usually represented by a thin, one-grain thick layer of pebbles or cobbles of variable lithology including metamorphic basement, pure quartz and sediment (Figure 3a). On the reg, sand accumulation only occurs as sand shadows or coppice dunes behind plants (Figure 5c). The direction of sand transport then corresponds to the direction of the long axis of the sand shadow. The size of these small structures varies, depending on the height and width of the associated bushes and, although the smallest ones generally indicate the direction of sand transport during the last strong-wind episode, we consider the largest ones, sometimes up to a meter in height, to be more perennial features representative of the mean direction of wind-blown sediment transport.

Finally, the Tsagaan Els depression hosts shallow aquifers mainly in the Upper Cretaceous formations and Quaternary deposits (Grizard et al., 2019). Grizard et al. (2019) demonstrated that the aquifers in the Upper Cretaceous series of the Zuunbayan sub-basin are controlled by the main central depression, with the water flowing from the edges of the sub-basin and discharging via subsurface evaporation in the central playa (Figure 4). In the Unegt sub-basin, the water in the

aquifer flows eastward toward a series of springs situated east of the Tavan Har basement high, along the North Zuunbayan fault (Figures 2 and 4).

2.2. Climate of the Tsagaan Els depression

Climate data were obtained using the Climate Data Online catalog of the U.S. National Oceanic and Atmospheric Administration for two weather stations: Sainshand (N44.900° / E110.117°, with data collected every 3 hours from August 1956 to May 2017) and Bayan Dobo Suma (N44.567° / E107.183°, with data collected every 3 hours from December 1973 to May 2017) in the NE and NW of the depression respectively (Figures 1 and 6). At both stations, the main wind direction is from the NW, with a limited spread between WNW and N, and a wind speed value generally between 10 and 35 $m.s^{-1}$ (Figure 6). The wind direction during storm events is similar to the overall wind direction, although a more westward component is observed. The temperature distribution shows a wide amplitude between about -20°C in winter and about +20°C in summer with extremes below -40°C and above 40°C. Precipitation data are only available for the Sainshand station and show that most precipitation occurs between June to August with a mean annual amount of only 59 mm over the considered period and some outliers up to 70 mm per month generally due to storms.

2.3. Methods for data acquisition

2.3.1. Description of the wind patterns

The wind pattern (speed and direction) in the Tsagaan Els depression was first investigated using the ERA-Interim project meteorological model which provides estimates of the wind speed and direction at altitudes of 10 m or 100 m above ground level (Simmons et al., 2007; Dee et al., 2011). However, this model has a 79 km grid resolution and does not account for wind perturbations due to local, small-scale topographic structures. To get a more accurate evaluation of the wind mean directions at ground level, we used field and satellite (see example study in Yao et al., 2007) measurements of the direction of propagation of the dunes and sand shadow features described above. This approach does not provide information about the wind speed. Direction values (measured clockwise from north) were gridded and interpolated using the "surface" calculation routine of the GMT Software (Smith and Wessel, 1990) to derive sand transport maps at ground level that we interpret as a proxy for wind direction. Note that the density of data is largely controlled by the occurrence of sand in the various regions of the basin which has a direct influence on the confidence level of the interpolation.

2.3.2. Cosmogenic nuclide dating methods

2.3.2.1. Sampling strategy

Cosmogenic nuclide analysis was used to derive the exposure age and erosion rates of the various surfaces in the depression. Pure quartz to quartz-rich samples were collected from surface lag deposits, sedimentary rocks or crystalline basement throughout the basin and especially around the eastern termination of the Tavan Har structure (Figures 2 and 4, Supplementary Figure 1 and Supplementary Table 1). Sampling sites were selected on flat surfaces, away from fluvial courses to prevent river-related slope diffusion that could locally increase the erosion rates. All sampled morphologies are erosion surfaces as lag deposit samples were collected from the reg-type soil described above, away from material that could have been brought by sheet-flood deposits. Except for sample M-61 in the main depression, no sample was collected from ephemeral lakes surfaces to prevent shading by water of fine-grained deposits linked to flooding. The local topography being largely low-relief sample shading by obstacles is limited (see Supplementary Table 1).

The samples were either single quartz cobbles about 10 cm in diameter, sets of about 50 quartz pebbles about 1 cm in diameter (quartz cobbles or pebbles found loose on the surface or as particles in sedimentary rocks are generally derived from eroded basement metamorphic veins) or granite and quartz vein chunks. This sampling was complemented by sampling of quartz-rich coarse-grained sedimentary rocks in three drilling sites (see below for detailed sedimentary logs of the three sections). Two of the sites were situated on the Bayanshire plateau, a preserved, isolated morphological surface in the Unegt Subbasin (Figure 2) possibly representing a remnant of the pre-incision topography of the basin. The third profile was excavated into the main depression being possibly representative of the most actively eroding part of the basin. Details on samples location and cosmogenic nuclides contents are available in Supplementary Table 1.

2.3.2.2. Dating methods

Sample preparation and measurement procedure follow the usual approach and are fully described in the supplementary file “Cosmogenic nuclides analysis”. Erosion rates and exposure ages were calculated using the classical equation of the nuclides production:

$$N(x,\varepsilon,t)=\frac{P_{neut.}\,e^{(-x\rho/\Lambda_{neut.})}}{\frac{\varepsilon\rho}{\Lambda_{neut.}}+\lambda}\left[1-e^{-t(\varepsilon\rho/\Lambda_{neut.}+\lambda)}\right]+\frac{P_{stop.}\,e^{(-x\rho/\Lambda_{stop.})}}{\frac{\varepsilon\rho}{\Lambda_{stop.}}+\lambda}\left[1-e^{-t(\varepsilon\rho/\Lambda_{stop.}+\lambda)}\right]$$

$$+\frac{P_{fast}\,e^{(-x\rho/\Lambda_{fast})}}{\frac{\varepsilon\rho}{\Lambda_{fast}}+\lambda}\left[1-e^{-t(\varepsilon\rho/\Lambda_{fast}+\lambda)}\right]$$

$$+N(0,\text{paleo}\varepsilon,\infty)\cdot e^{(-\lambda\cdot t)}\quad\text{Equation 1.}$$

A SLHL spallation production of 4.02 ± 0.33 atoms g^{-1} a^{-1} (Borchers et al., 2016) was used and scaled using Stone polynomial (Stone 2000) and Cosmocalc Excel add-in (Vermeesch, 2007). Muon contributions of Braucher et al. (2011) were applied. The $^{26}Al/^{10}Be$ production ratio induced by the standardization used at ASTER (SM-Al-11/07KNSTD) is 6.61±0.50 (Rixhon et al., 2011).

From the measurement of the concentration of two cosmogenic nuclides (^{10}Be and ^{26}Al) in a single sample, the three unknowns (paleo-erosion rate: paleoε, erosion rate: ε and exposure age: t) from Equation 1 (see Supplementary file "Cosmogenic nuclides analysis" for details) cannot be determined simultaneously since the equations used for each of the cosmogenic nuclides contain the same unknowns. Therefore, two options are possible (Supplementary Table 2). First, considering no inheritance (simple exposure history), where using Equation 1 to allow modeling both the exposure age (t) and the erosion rate (ε). Following this approach, concentrations increase with time until they reach a constant value when the gains by production equal losses by radioactive decay and erosion. The time needed to reach this plateau value, the integration time, directly depends on the erosion rate and marks the theoretical limit of the dating method: it is impossible to date beyond this integration time. Secondly, considering a complex exposure history where "burial", paleo-erosion (paleoε) and exposure age (t) can be determined assuming no production after deposition. In that case, the resulting age will be minimum. As discussed in section 4.2, this "burial" can in fact only be virtual and result from a change in the erosion rate which induces a variation in the $^{26}Al/^{10}Be$ ratio similar to that resulting from a burial.

These two options will allow bracketing of the denudation rates and exposure ages. All outputs presented in this study consider both ^{10}Be and ^{26}Al measurements together. However, to provide a full analysis of the data, the classical maximum erosion rates (considering infinite time) and minimum exposure ages (no erosion) considering one nuclide have been presented in Supplementary Table 2 as well as the same approach of maximum erosion rate considering both nuclides. The latter option, considering maximum erosion rates, results in more difficulties in reproducing the data.

Finally, because both ^{10}Be and ^{26}Al nuclides are produced in the same mineral and thus have undergone the same exposure history since they were emplaced in the sedimentary rock, it is possible to analyze multiple samples from a vertical profile to determine more than two unknowns. In that case the paleo-erosion (paleoε) that affected each profile sample before its burial, and both the erosion rate (ε) and the exposure time since the deposition event (t) can be determined with a

minimum of two samples. For all samples from a given depth profile, these two latter unknowns are identical.

3. Results

3.1. Wind pattern from ERA-Interim data (10 m)

Mean wind pattern (direction and speed at an altitude of 10 m above the ground) have been calculated for 3 different months based on the ERA-Interim model (Figure 7). In general, the calculated wind speed is maximum in the central part of the Unegt Basin, immediately in front of the Tavan Har structure and decreases on the lee side of the basement high in the Zuunbayan Basin before increasing again on reaching the Totoshan Ridge to the south. As expected, streamlines show a marked deflection produced by the Tavan Har topography. The wind blowing from the north in the Unegt Basin (a direction mainly consistent with the meteorological observations presented above) is either simply deflected toward the SE (see the June 2016 example on Figure 7) or, more generally, forms vortices on the lee side of the NE and SW terminations of the Tavan Har massif and flow reversal develop in the Zuunbayan Basin creating a complex wind pattern.

As dust and sandstorms associated with strong winds are known to be a major factor influencing soil erosion and sand movement in the southern Gobi region (Middleton, 1991; Natsagdorj, 2003; Kapp et al., 2015), we also calculated wind pattern maps (wind at an altitude of 10 m above ground) for three days corresponding to large storms (storm days have been selected using the meteorological data available for the Sainshand Station as described above). Although the compilation of strong wind data registered at Sainshand weather station indicate NW to WNW winds (Figure 6), the three ERA Interim derived maps show mostly a W to WNW wind direction on the western side of the Tsagaan Els depression, rotating NE in the eastern part of the basin. Except for that rotation, the storm-wind pattern appears homogeneous without the relief-dependent disturbances observed in the monthly averages. Finally, the modeled storm wind direction is poorly to not compatible with the direction of propagation of the major dune fields in the depression (see below).

3.2. Aeolian sand transport around the Tavan Har structure

Measurements of the sand transport direction have been interpolated to produce a large scale map of sand motion within the Tsagaan Els depression (Figure 8). It should be noted that this map largely relies on the density of data and most of them were obtained in the close vicinity of the Tavan Har

structure. In most of the Unegt sub-basin, the transport direction is NW to SE, corresponding to the measured mean wind direction at Sainshand and Bayan Dobo Suma stations (Figure 6) and oblique compared to that predicted by the ERA-Interim model (Figure 7). In the Zuunbayan sub-basin, the wind direction changes towards close to westerly before switching again towards a more WNW direction on the Totoshan ridge to the south. This last direction corresponds to that of a major dune field separating the Zuunbayan sub-basin from the Erdene valley to the East (Figures 1 and 4). West of the Zuunbayan sub-basin, the transport direction is largely W-E, marked again by a large dune field. Again, in these two locations, the measured sand transport directions are oblique to the wind direction predicted by the ERA-Interim model although not entirely incoherent. Figure 8b is a closer view of the interpolated sand transport directions around the Tavan Har structure. As indicated above, the transport direction is largely constant towards the SE in the Unegt sub-basin as well as on the conical structure north of the basement high. Towards the NE, where the slope of the cone decreases, the transport direction changes towards a nearly W-E direction before establishing back to the SE away from the termination of the basement high. On the southern side of the Tavan Har hill, the transport direction varies from NW-SE to W-E indicating a strong topographic control on wind direction. The topographic depression south of the NE termination of the basement high is characterized by sand moving towards the E. In the depression to the SW, less documented due to the near absence of sand (the ground is largely covered by a gravel to pebble pavement), the transport direction is WNW-ESE.

Based on those observations, it appears that the large Mandakh-Saykhandulaan ridge north of the Tsagaan-Els depression has no or only a minor effect on the wind direction in the Unegt sub-basin (this one remains consistent with the regional wind direction). These winds probably have a katabatic component and increase in speed as flowing down into the basin. However, the measurements confirm that the Tavan Har basement high exerts a major control on the wind pattern inside the Zuunbayan sub-basin.

3.3. Erosion rates and chronology inferred from in situ-produced concentrations of the cosmogenic ^{10}Be and ^{26}Al nuclides

3.3.1. Surface samples

The modeled erosion rates calculated from cosmogenic nuclides data as well as their Kernel density plot (Vermeesch 2012) are presented in Figure 9 while associated ages are reported in

Supplementary Table 2. Note that the value implemented for a given sample in the Kernel density calculation (Figure 9b) has been selected considering the best fitting result from option 1 or option 2. This best fit was determined using the highest probability of $\chi^2 = ((N_{measured} - N_{modeled}) / \sigma_{measured}))$, $\sigma_{measured}$ being the uncertainty associated to the measured concentration ($N_{measured}$), determined for each calculation result (Supplementary Table 2). In most cases, the two-options yield similar long-term erosion rates ranging from 0 to 49.3 m/Ma. Ignoring this latter extreme value, the Kernel curve exhibits two maxima, one at ~7 m/Ma, the second at ~20 m/Ma. The two types of samples (multiple pebbles versus single cobble) lead to consistent results. However, the erosion rates of 7 surface samples are significantly different (the names of these samples are indicated on Figure 10). This may be due either to heterogeneity in the amalgamated samples or to a different exposure history that may involve partial burial of single cobbles. The heterogeneity refers here to the potential presence in the amalgamated sample of one or several pebbles with anomalously high (or low) concentrations that shift the mean concentration calculated from the whole pebble population.

Samples from the Totoshan ridge, as well as from a small basement high above the southern edge of the Zuunbayan sub-basin, yield erosion rates between 0 and 10 m/Ma (Figure 4). Samples MN17-50 and MN17-53 yield erosion rates slightly higher than 10 m/Ma, but they are situated on a sedimentary surface at the base of a 50 m high cliff. The top of the cliff is affected by erosion rates lower than 5 m/Ma (samples MN17-51 and MN17-52), indicating large variations at a small local scale. To the north of the study area, on the large fan-terraces system that separates the Mandakh-Saykhandulaan ridge from the lowest part of the depression in the Zuunbayan sub-basin, erosion rates vary from less than 5 m/Ma up to nearly 20 m/Ma.

However, the most scattered results were obtained around the Tavan Har structure. Samples MN17-1 and MN17-2 with erosion rates of 26.13 ± 3.38 m/Ma and 31.53 ± 3.05 m/Ma, respectively, were collected from the top of a conglomerate ridge immediately north of the North Zuunbayan fault. This ridge forms the northern boundary of a depression (several hundred meters across and tens of meters deep) developing between the basement and the Cretaceous strata. Immediately to the north, samples MN17-3 to MN17-5 were collected along the slope of the conical structure. They yield higher erosion rates, increasing towards the top of the structure. Samples MN17-7 and MN17-8 were collected in the ephemeral lakes that form the local base level at the foot of the conical surface. They provided some of the highest erosion rates at around 20 to 25 m/Ma. South of the eastern termination of the Tavan Har basement, samples MN17-31 and MN17-32 were collected on the plateau forming the summit of the basement high. Sample MN17-31 is a quartz vein in the gneiss while sample MN17-32 is a surface quartz cobble. They lead to erosion rates of 6.24 ± 3.24 and

4.22 ± 0.63 m/Ma, respectively, similar to those obtained on the Totoshan ridge. Sample MN17-34 was also collected on the southern edge of the plateau but on the edge of a small, 30 m large and 10 m deep canyon which might explain its higher erosion rate of 14.39 ± 5.22. Finally, on the south-western edge of the main depression zone in the Zuunbayan sub-basin, sample MN17-61 records an intermediate erosion rate of 10.38 ± 0.79 m/Ma.

Regarding the ages obtained through the two approaches (Supplementary Table 2), they significantly vary depending on the selected modeling option, unlike the erosion rates. In addition, considering the simple exposure model (one nuclide), the calculated ages may be considered as too old to be compatible with the calculated erosion rates. Indeed, the integration times (considering all particles involved i.e. neutrons and muons) range from 2 Ma for an erosion rate of 0 m/Ma down to ~30 ka for a ~50 m/Ma erosion rate (the erosion range obtained in this study), making them higher than those which theoretically cannot be exceeded.

Considering the paired ^{10}Be and ^{26}Al, these offer the possibility to have a perfect match between the modeled and measured concentrations because the time considered is not only the time needed to accumulate the nuclides but also the time needed for the produced nuclide to decay.

When both modeled options yield to the same erosion rate, an agreement is also observed when looking at maximum erosion rates deduced from individual nuclides (see Supplementary Table 2). In that case a simple exposure history is to be favored.

3.3.2. Depth profiles

The ^{10}Be and ^{26}Al concentrations were measured along three depth profiles dug into the basin for this purpose (Figure 11 and Supplementary Table 1). Profiles P1 (samples MN17-10 to MN17-19) and P2 (samples MN17-36 to MN17-45) are situated on the Bayanshire plateau, an isolated, perched morphological surface located immediately NE of the eastern termination of the Tavan Har structure. This erosion surface is cutting through the Upper Cretaceous Bayanshire deposits and displays two sub-surfaces: a low sub-surface to the S in which profile P1 was sampled and a high sub-surface to the N in which profile P2 was sampled. Although no evidence of active deformation could be obtained from field investigation, the scarp separating the two sub-surfaces coincides with the mapped trace of the North Zuunbayan fault (Figure 11).

The low sub-surface (profile P1) is flat with only a few small dunes along its eastern edge and no evidence of river incision. It is paved by centimeter-size, moderately wind-polished pebbles of quartz and metamorphic rocks. The section exposed along the cliff at the southern edge of the subsurface suggests that the post-Cretaceous deposits are less than a meter thick. Indeed, the upper

first 30 cm of the logged section, hereafter referred as the active layer, are discordant on the underlying series and mainly composed of poorly consolidated fine-grained sand with 3D mega-ripples corresponding to dune deposits. The second unit, from 30 to 165 cm depth, is made of coarse-grained sandstones including centimeter-thick lenses of rounded pebbles, alternating with decimeter-thick carbonate-cemented gravel beds, including some loose pebbles and showing erosive bases. The unit is markedly impregnated by a carbonate cement with lenses of strongly cemented sand. 3D mega-ripples and horizontal laminations are observed. This unit is interpreted as fluvial deposits belonging to the Upper Cretaceous Bayanshire Formation.

The high sub-surface (profile P2) is more dissected, affected by several shallow fluvial incisions. It is paved by centimeter to decimeter-size pebbles and blocks of quartz and metamorphic rocks. The logged section is composed of 2 units. The first 25 cm of the upper unit 1 is composed of poorly sorted medium-grained sandstones with a few lenses of coarse-grained sandstones and gravels. Faint 3D mega-ripples are visible. The next 30 cm beneath are massive coarse-grained sandstones with few gravelly layers and loose pebbles, strongly consolidated by a carbonate cement. The base of that layer is eroding into a centimeter-thick and strongly oxidized layer interpreted as a paleosol. The bottom 15 centimeters of unit 1 is composed of horizontally laminated coarse-grained sandstones. Unit 1 is interpreted as low-energy alluvial plain deposits. A second unit characterized by 10 to about 30 cm-thick layers of gravels and coarse-grained sandstones with loose pebbles and cobbles extends from 70 to 190 cm. The base of each layer displays a sharp contact with the underlying deposits indicating syn-sedimentary erosion. The unit is interpreted as channel deposits in an alluvial plain, again belonging to the Upper Cretaceous Bayanshire Formation.

Profile P3 (samples MN17-61 to MN17-71) was sampled on the edge of the large ephemeral lake system forming the main depression of the Zuunbayan sub-basin (Figure 11). The aim was to obtain erosion rates and/or surface ages in the lowest part of the basin. The surface in which profile P3 was excavated is characterized by meters-high aeolian dunes alternating with sand-free patches of red siltstone. The latter are covered by a near continuous one-grain thick layer of highly rounded gravels, 3 to 5 millimeters in diameter. The first 50 cm of the logged section are composed of massive red clay-rich siltstone including thin layers of coarse-grained sandstones. Mud cracks indicate drying periods between flooding events and these sedimentary facies are characteristic of the ephemeral lake. Below that first unit, the strata are composed of massive fine-grained sandstones showing fluvial 3D trough cross-bedding (Williams, 1968). Carbonate nodules are present within the uppermost 5 cm of that second unit. One to 5 cm-thick layers of coarse-grained sandstones and gravels, some showing erosive bases, are regularly intercalated. This unit is

interpreted as an arid alluvial plain deposit associating water-reworked sand dunes and small channels. The connection of the lower part of the profile to the Cretaceous series is more difficult to assess.

Profile 1 concentrations (Supplementary Table 1) are significantly higher at a given depth than those measured along Profiles 2 and 3 which both exhibit roughly similar cosmogenic nuclides concentrations. As shown in Figure 12, the evolution as a function of depth of the ^{10}Be and ^{26}Al concentrations of all the samples, except for the lower concentrations of the second sample of each profile (MN17-11 and MN17-37 at 5 cm) as well as of sample MN17-62 at 20 cm in the Profile P3, exhibits the same pattern which corresponds to the expected exponential decrease. Highlighted for both ^{10}Be and ^{26}Al and for the three depth profiles, these lower concentrations cannot be considered as outliers but most likely have a geomorphic explanation.

The sedimentary sections corresponding to each profile (Figure 11d) display a surficial centimeter-thick layer of small gravels to pebbles. This layer covers a 10 to 30 cm sandy layer that itself overlays the highly lithified Cretaceous strata in profiles 1 and 2. It seems that the sandy layers (active layer) in which MN17-11 (Profile 1), MN17-37 (Profile 2) and MN17-62 (Profile 3) have been sampled are affected by higher erosion rates that decrease the cosmogenic nuclides concentrations. Surprisingly, although belonging to the active layer, the surface sample concentrations are part of the expected exponential decrease, implying that the top pebble layers can be modeled with the same parameters (erosion, exposure time) than the samples originating from the indurated sediment unit. To better model the depth profiles we propose a new approach presented hereafter in Equation 2:

$$N(x,\varepsilon,t) = \frac{P_{neut.}\, e^{(-x\rho/\Lambda_{neut.})}}{\frac{\varepsilon\rho}{\Lambda_{neut.}}+\lambda}\left[1 - e^{-t(\varepsilon\rho/\Lambda_{neut.}+\lambda)}\right] + \frac{P_{stop.}\, e^{(-x\rho/\Lambda_{stop.})}}{\frac{\varepsilon\rho}{\Lambda_{stop.}}+\lambda}\left[1 - e^{-t(\varepsilon\rho/\Lambda_{stop.}+\lambda)}\right]$$

$$+\frac{P_{fast}\, e^{(-x\rho/\Lambda_{fast})}}{\frac{\varepsilon\rho}{\Lambda_{fast}}+\lambda}\left[1 - e^{-t(\varepsilon\rho/\Lambda_{fast}+\lambda)}\right] + N(x, paleo\varepsilon, \infty)\cdot e^{(-\lambda\cdot t)} \quad \text{(Equation 2)}$$

where the term N(0, paleoε,∞) of Equation 1 has been replaced by N(x, paleoε,∞), x being the sample depth.

This is justified because these deposits are Cretaceous and therefore the ^{10}Be and ^{26}Al concentrations accumulated in the samples before their deposition in the studied profile (first inheritance) have decayed radioactively. Thus, the paleo-erosion rates determined in that case are not those prevailing before deposition but those prevailing after the deposition event, leading to exhumation of those Mesozoic series. Changing Equation 1 to Equation 2 only affects the paleo-erosion rates and not the exposure ages and erosion rates. The best-fit solutions are presented in Supplementary Table 3 and in Figure 13. Uncertainties on paleo-erosion rates range from 0.5 to 1 m/Ma. Including or excluding the top surface sample from the calculation has an impact on the model outputs, especially regarding Profile 1. Therefore two groups of solution are proposed, with or without the top sample (Supplementary Table 3).

When considering the top samples into the calculation, the best fits for the three depth profiles lead to the similar exposure ages within uncertainties, the age deduced from Profile 3, nevertheless, is seemingly younger. However, major discrepancies are highlighted while analyzing the erosion and paleo-erosion rates. Regarding Profile 1, the erosion rate is 18.1±1.2 m/Ma and the paleo-erosion rates range from 1.2 to 6 m/Ma for the indurated Cretaceous unit and top samples with a median value of 3.3 m/Ma. The paleo-erosion and erosion rates deduced from the active layer samples are similar (~25 m/Ma). Profiles 2 and 3 exhibit similar erosion rates (~10m/Ma) but significantly different paleo-erosion rates. Erosion rates from Profile 2 range from 14.5 to 39.8 m/Ma with a median value of 22.8 m/Ma, whereas those from Profile 3 range from 1.1 to 51.1 m/Ma with a median value of 3.7 m/Ma. Regarding Profile 3, the top sample and the sample in the active layer has no evidence for inheritance. Regarding Profiles 2 and 3, the active layer samples reveal erosion rates of 102.2 and 18.0 m/Ma, respectively, higher than the erosion rate derived from the deeper samples.

Alternatively, considering the top samples as outliers and excluding them from the calculation, has no effect on Profile 2, a limited effect on Profile 3, but has a considerable effect on Profile 1 for which the erosion rate decreases to 5.6±0.2 m/Ma and the exposure age markedly increases to 1.64±0.45 Ma.

4. Discussion

4.1. Fluvial and aeolian interactions in geologically complex depressions: a conceptual model

The erosion pattern in a natural depression developing upon a substratum with contrasted erodibility implies strong interactions between fluvial mobilization and transport of detrital material and aeolian deflation and transport of the finer particles. Unlike in large pans such as the Etosha pan in Namibia (Hipodonka, 2005; Miller et al., 2010) or in wide sedimentary basins such as the Qaidam Basin in Tibet and China or the Lut Basin in Iran (Ehsani and Quiel, 2008; Heermance et al., 2013; Rohrmann et al., 2013), the occurrence of lithological contrasts generates erosion-resistant relief that form wind obstacles (Ruszkiczay-Rüdiger et al., 2011, Sebe et al., 2011).

The kinematics of airflow around topographic obstacles has been largely studied both theoretically and experimentally (Castro and Robins, 1977; Hunt et al., 1978; Smyth, 2016; Liu et al., 2019). The Tavan Har basement high, excluding the conical structure on its northern face is a flat-topped elongated structure with high aspect ratios of 2.75 and 80 for lengths versus width and height versus width respectively. The models addressing the surface flow structure over oblong artificial piles of granular material and natural ridges (Badr and Harion, 2005, 2007; Furieri et al., 2012; Liu et al., 2019) or transverse dunes (Jackson et al., 2013; Courrech du Pont et al., 2014; Smyth, 2016) are thus of particular interest to explain the erosion pattern in the Tsagaan Els depression. On a flat, smooth terrain, the wind flow interacting with a laterally limited oblong obstacle perpendicular to flow direction displays some characteristic features (Badr and Harion, 2005, 2007; Furieri et al., 2012):

1- As for all obstacles, the increase in pressure on approaching the obstacle induces a deceleration of the flow. Since the wind transport capacity of sand particles is related to the wind speed (Bagnold, 1941), such deceleration should lead to deposition. When the change in slope at the toe of the obstacle is sharp, this phenomenon is partially compensated by the formation of turbulence that can produce enough shear stress to allow some transport (Hunt et al., 1978; Wiggs et al., 1996). The wind flow then accelerates upslope as pressure drops, inducing a maximum shear stress along the windward crest of the obstacle (Badr and Harion, 2005) thus increasing the erosion potential.

2- On the lee side of the obstacle, two counter-rotative and symmetrical vortices develop, leading to the formation of a low-shear stress region. Vortices form when the flow accelerated upslope of the upwind side of the obstacle detaches from the surface and interact with the slow-motion wind behind the obstacle. The strength of the vortices depends upon the difference in velocity and pressure between the two fluids (Hunt et al., 1978; Badr and Harion, 2005). The resulting triangular-like region of low shear stress is marked by deposition, a good example being the sand shadows and coppice dunes accumulated behind bushes (Figure 5C).

3- The major perturbation in wind flow is a strong increase in shear stress on both ends of the obstacle, reaching a maximum value immediately downstream the extremities. In that region, the flow is accelerated on the upwind region and this acceleration adds to the downward motion of the flow in the vortices that form behind the obstacle (Badr and Harion, 2007; Furieri et al., 2012). Those regions, immediately behind each side of the obstacle are thus the locus of the maximum erosion. The shape and size of the acceleration zone is highly sensitive to the angle between the direction of the upcoming wind and the obstacle (Turpin and Harion, 2010; Furieri et al., 2012).

We suggest that these three main perturbations in the wind flow account for the morphology of the Tsagaan Els Basin (Figure 14). The conical structure configured within the Cretaceous strata on the northern side of the Tavan Har high is indeed covered by a thin active layer of aeolian sand – including small dunes – that disappears progressively upslope except in the extreme northeastern part of the massif where the sand sheet continues on the summit plateau (Figure 2). Similarly, to the southwest, sand also reaches the summit of the massif however in a much smaller amount. Erosion rates calculated from the cosmogenic nuclide analysis also increase from the bottom to the top of the slope, reaching a regional maximum of 30 to 35 m/Ma on the crest (samples M-2 and M-8) (Figures 2 and 4). Sample M-7 was also collected near the crest line of a small basement high that crops into the low part of the basin, probably explaining its relatively high erosion rate compared to samples M-5 and M-6 in the same position. These sand and erosion rate distribution patterns appear to match the theoretical model except that the location of the arcuate depression containing the ephemeral lakes at the toe of the conical structure north of the massif does not fit a decelerating flow. We suggest that the northern part of the Unegt Basin is situated within the pressure shadow developing on the lee side of the Mandakh-Saykhandulaan ridge. The maximum wind velocity is thus reached in the central part of the basin where the small depressions filled with ephemeral lakes develop, away from the ridge shadow and before reaching the Tavan Har massif. Relative to the other erosion rates obtained in the basin, that area is marked by high erosion rates of 20 to 25 m/Ma (Figure 4). Nonetheless, these rates remain low compared to values obtained in similar deflation studies such as 40 – 60 m/Ma in the Pannonian Basin (Ruszkiczay-Rüdiger et al., 2011) or 120 – 1100 m/Ma in the Qaidam Basin (Kapp et al., 2011; Rohrmann et al., 2013). The ERA-Interim model (Figure 7) also suggests a maximum wind speed in the center of the Unegt Basin and a decrease on approaching the Tavan Har massif. Nonetheless, the model resolution does not allow imaging the upslope acceleration. Aeolian processes possibly initiated the formation of the depression in front of the Tavan Har massif, creating local base levels that triggered the formation of a new set of fluvial drainage systems eroding the southern slope of the Mandakh-Saykhandulaan

ridge. Arid to semi-arid floodplains are major providers of fine-grained material to aeolian dune fields (Bullard and Livingstone, 2002; Bullard and McTainsh, 2003; Belnap et al., 2011). The ephemeral nature of all the rivers forming the drainage system in the Tsagaan Els depression leads to the deposition of thin planar sheets (flood sheets) or lobes of mud-supported sand, pebble and /or cobble conglomerates depending on the material available in the drainage system and on the water discharge (Dill et al., 2005). Due to the high rates of sediment supply during these discharges, and to their rapid flood recession characteristics, the surface of the deposits is poorly armored by the largest grains facilitating deflation of the silt and fine to medium sand fractions during dry intervals (Lisle and Hilton, 1992; Yao et al., 2007; Powell, 2009). Removing of the finest granulometric fraction through deflation typically produces the reg-type surfaces observed throughout the depression. The relatively fine-grained lithology of the Mesozoic series forming the substratum of the Tsagaan Els depression further enhances the production of sandy and silty material which is finally removed from the endoreic sub-systems by deflation. Finally, the ephemeral lakes that form the most distal part of the drainage sub-systems may also play a major role in facilitating material export through winnowing. Playas can be major dust providers for several reasons. For example, wet playas are generally characterized by a salt layer on the surface, which, mixed with silt and clay represent material easily mobilizable by wind during dry periods (Reheis and Kihl, 1995; Reheis, 1997; Reynolds et al., 2007; Reheis and Urban, 2011). Fine grained material generally deposited in the playa is not only easily transported by wind but is also easily mobilized by abrasion from saltating sand grains. This last phenomenon may be increased by the occurrence of bushes creating wind disturbances that increase the local shear stress (Pelletier, 2006). The present-day low annual precipitation favors deflation against fluvial sedimentation preventing the local depressions from being filled by fluvial sediments. Following these mechanisms, the increased deflation in the main depression of the Zuunbayan subbasin may partly explain the occurrence of the large dune field that has developed immediately SE of the major playa (Figures 1 and 4). Along the slope connecting the Mandakh-Saykhandulaan ridge with the central depression, sampling has been undertaken to avoid river channels so that the measured erosion rates reflect the surface erosion and not the activity of the intermittent channels. Nonetheless, some of the samples may still be affected by increased slope diffusion in the vicinity of large channels that was impossible to prevent during sampling. The heterogeneity observed in the erosion rates along that general slope reflects the strong increase of erosion capacity between the wind erosion characterized by low rates of 0 to 10 m/Ma (dark and light blue points on Figure 4) and erosion rates up to 20 m/Ma combining river-associated slope-erosion processes and wind deflation (light green points on Figure 4).

The NE and SW depressions mapped immediately behind the Tavan Har massif correspond to the expected zone of combination between the flow acceleration around the extremities of the obstacle (Figure 2) and the down-flow region of the vortex that forms on the lee side. The mean wind direction in the Unegt Basin (blowing from N315°) is slightly oblique through to perpendicular to the front of the Tavan Har massif (N330°), which, based on numerical models, should favor the northeastern high wind shear stress zone (Furieri et al., 2012). The direction of sand motion in the large sand sheet reaching the plateau to the NE clearly indicates a rotation in the wind direction from SE to E in accordance with the flow pattern observed on models (example.g., Furieri et al., 2012). To the NE, this region is also marked by highly variable sand-transport directions suggesting the formation of turbulence (Figure 8). The flow velocity and associated shear stress increasing from the axis of the massif towards the extremities, the deflation and abrasion capacities also increase ultimately carving the conical structure on the upwind side of the Tavan Har massif. A fluvial system developed on the conical structure (Figure 2), bringing loose material to the toe of the slope where wind shear stress and thus deflation is maximum. It should be noted that the increase in flow velocity associated to the extremities of the massif is not defined on the ERA-Interim model (Figure 7) and the vortices observed in the model are not superposed with the NE and SW secondary depressions. This discrepancy is probably related to the low resolution of the model compared to the high frequency – low amplitude roughness of the topography (canyons or local highs in the basement for example).

The two vortices as well as the lower flow velocity on the lee side of the massif are well defined on the ERA-Interim model (Figure 7, April 2019 and October 2016 panels). No major sand deposits are exposed behind the central part of the Tavan Har massif where such a wake zone should be expected, although small dunes and sand shadows are present and sand motion directions are clearly turning before coming back to the initial NW direction away from the massif (Figure 8). Topographically, the axial region of the lee side is slightly higher than the surrounding Zunnbayan Basin, corresponding to a drainage divide between rivers flowing towards the main depression to the NE and a low point to the SW. Along the southern limit of the crystalline basement, present-day rivers are also flowing NE and SW from the axial zone, transporting loose material to the secondary depressions on each end of the massif. This material is then deflated by wind, maintaining the depressions as low points.

Based on the results derived from in situ-produced cosmogenic nuclide concentrations in both surface and profile samples, we infer that the dynamics of the erosion system in the Tsagaan Els depression may be also linked to climate changes. The area may have experienced a marked change

in erosion rate from a value probably lower than 5 m/Ma (many surface samples erosion rates as well as paleo-erosion rates derived from Profile 1 and 2 favor this value) to a rate higher than 10 m/Ma.

The erosion mechanism described above in the Tsagaan Els depression should apply to other depressions developing under semi-arid to arid climates but could also be complemented by processes evidenced in those regions. As already mentioned above, many studies have addressed the dynamics of aeolian transport in the western United States (California, Colorado and Utha, especially focusing on the source of the material, the production of dust and the effects of climate or anthropogenic changes (Muhs et al., 1996, 2003; Reheis, 1997, 2006; Reynolds et al., 2007; Reheis and Urban, 2011). This region is topographically complex, including numerous basement massifs surrounded by valleys hosting large dune fields. Based on the results presented above and although it might not be easy to determine, the detailed wind pattern should be considered to evaluate maximum deflation zones. In Africa, Wormald et al. (2003) established that the spatial distribution of pans in the Kalahari Desert of Botswana is correlated to the occurrence of basement faults, the pans developing upon unconsolidated sands. Similarly, the still poorly understood Qattara depression in Egypt was developed within Cenozoic strata displaying lithological contrasts and tectonic fractures. To the north, upwind, the depression is limited by a cliff separating the basin from a plateau capped by carbonate rocks while the strata exposed in the depression are mainly clastic (Albritton et al., 1990). Rivers perpendicular and parallel to the cliff (Bassler, 1968) are mobilizing clastic material inside the depression that feed dune fields to the south. Recently, McMillan and Schoenbohm (2020) related the formation of a large depression in the Puna Plateau (Argentina) to wind abrasion and deflation. However, they suggest that fluvial incision and transport played a minor role due to the hyper-arid climate. Finally, Pullen et al. (2018) describe large-scale wind erosion (including abrasion and deflation) in the Hami Basin (NW China) suggesting that the wind intensity may be controlled by the low albedo of the dark-gravel armored basin floor. Although the Hami Basin is again a hyper-arid region, ephemeral drains remain active and could participate in the erosion by disturbing the gravel pavement.

4.2. Climate change and the onset age of the present-day erosion mechanism in the Tsagaan Els depression

Based on the results deduced from in situ-produced cosmogenic nuclide concentrations in both surface and profile samples, we infer that the kinematics of the erosion system in the Tsagaan Els

depression is also linked to climate changes. Supplementary Table 2 shows that, for surface samples, when the measured age does not fit the modeled age ($\chi^2 > 0$) considering option 1, it does fit the modeled age using option 2 (or vice versa, except for a few samples). However, for option 2, the complex exposure approach is designed to determine burial ages (Granger and Muzikar, 2001; Granger 2006) and burial should not apply to those samples that clearly represent a newly formed active layer above the underlying substratum.

One possible explanation is a change in erosion rate. The landscape may have been first exposed for a long time at a certain erosion rate. Then, due to climatic or topographic disturbances, the long-term erosion rate may have changed towards a higher one. Theoretically, if the erosion rate decreases, the cosmogenic nuclide concentrations (^{10}Be and ^{26}Al) should increase to reach new, higher equilibrium concentrations. The ^{26}Al/ ^{10}Be ratio would thus evolve along the steady state limit of the erosion island defined by Lal (1991, Figure 15). If the erosion rate increases, the cosmogenic nuclide concentrations (^{10}Be and ^{26}Al) accumulated during the previous step with lower denudation should decrease to reach new, lower equilibrium concentrations. The ^{26}Al/^{10}Be ratio would then evolve in the burial area (below the steady state erosion island defined by Lal, (1991)). This is illustrated in Figure 15 with an erosion rate change from 3 m/Ma (many surface sample erosion rates and Profile 1 and 2 paleo-erosion rates indicate values lower than 5 m/Ma) to 10 m/Ma (the lower value observed in surface samples from the most actively eroding areas). This increase in erosion rate results in an apparent burial as long as the new equilibrium concentrations are not reached. As this concentration decrease involves radioactive decay, the time needed to "travel" from the starting point to the final one can be on the order of several million years (Figure 15). Following that model, the 1.64±0.45 Ma exposure age calculated on Profile 1 using the solution excluding the top sample (see section 3.3.2) can be explained as the time needed to decrease (mainly by radioactive decay) the inherited component acquired in the Profile 1 samples before the erosion rate changes.

The actively eroding regions of the studied area thus probably experienced a change in erosion rate from an initial, regional low range of 1-8 m/Ma to a locally higher range of 18-22 m/Ma. This may explain the bimodal Kernel distribution of the erosion rates (Figure 9). Based on the exposure ages determined from the depth profiles, this shift in erosion rate may have occurred 0.7 Ma ago, corresponding to the end of the middle Pleistocene transition (Clark et al., 2006; Sun et al., 2019). This age is also within the 0.4 to 1.1 Ma range of exposure ages calculated following option 1 for the high erosion rates samples on the northern front of the Tavan Har massif (MN17-01 to MN17-08, except MN17-05 for which the erosion rate is very low). This period corresponds to a major

change in the frequency of glacial cycles during the Quaternary that resulted in an increase in Asian aridity and winter monsoonal intensity, enhancing soil degradation (less vegetation coverage (see for example Belnap et al., 2009 or Laity, 2013) and aeolian deflation (Clark et al., 2006; Han et al., 2012; Cai et al., 2014; Wang et al., 2020). Similar enhanced aeolian deflation has been reported from the Qaidam Basin (N Tibet, China) during glacial and stadial periods following the Middle – Late Pliocene drying of the large lake system formerly filling the basin (Kapp et al., 2011). After 1.2 Ma, due to the generally drier climate and to tectonic activity, lakes in the Qaidam Basin were restricted to small fold-controlled depressions and frequently dried forming playas and locally increasing the deflation rates (Heermance et al., 2013).

4.3 Possible effects on the aquifer pattern of semi-arid depressions

The shallowest aquifers of the Tsagaan Els depression are tightly controlled by the position of the topographic low points (Figures 1 and 2) (Grizard et al., 2019). The strong deflation in the main central depression of the Zuunbayan sub-basin thus clearly influences the flow pattern in the corresponding aquifers. In response, the position of the water table may also control the deflation rate in the playas: surface deflation is lower in dry playas (water table at least 5 m below the surface) than in wet playas because the lack of interaction between the ground water and the surface prevents the formation of a surficial salt-rich easily erodible layer (Rosen, 1994; Reynolds et al., 2007). However, continuous deflation in the secondary depression developing around the eastern corner of the Tavan Har basement high may lead to the formation of a new evaporation-controlled discharge area, modifying the flow in the aquifers. The location of the preferential deflation zones probably changed through time, controlled by the modifications in the wind-flow pattern themselves linked to the evolution of the general topography. In correlation, it can then be assumed that the location of the aquifer discharge zones have changed through time, modifying the shape of the underground flows. Furthermore, during wetter periods, the various depressions may be filled by lakes, again modifying the hydrological framework of the basin but also the erosion – deflation pattern. Indeed, the occurrence of lakes will suppress the role of the playas as dust sources and preferential deflation zones. This general increase in moisture and the probable stronger vegetation cover should favor fluvial processes and decrease aeolian deflation (Wolfe and Nickling, 1993; Bullard and Livingstone, 2002; Reynolds et al., 2007).

These processes require further exploration. Basins developed under semi-arid to arid climate regimes, and especially those evolving in an endoreic setting, are highly sensitive to climate changes and anthropogenic activities (Laity, 2003; Pelletier, 2006; Yapiyev et al., 2017; Wang et al.,

2018; Sankey et al., 2018b), one well-known example being the drying Aral sea in Central Asia. The data presented in this study suggest that not only the surficial water bodies but also the aquifers may be affected by changes in deflation patterns leading to complex issues in water management.

5. Conclusions

The erosion and sedimentation pattern in topographically and geologically complex arid to semi-arid depressions is controlled by the close interplay between aeolian and fluvial processes. Unlike most large pans that develop upon a relatively homogeneous sedimentary substratum, the erosion pattern in such depressions is complex with preferential deflation zones controlled by the occurrence of erosion-resistant relief in mechanically less resistant sedimentary series. The use of ERA-Interim reanalysis wind model complemented by field mapping of the sand displacement vectors around the Tavan Har basement high allows for a direct analogy between the wind pattern around that natural, large scale obstacle and the wind pattern predicted by theoretical analysis and numerical or analog modeling around a laterally limited oblong obstacle perpendicular to the wind flow. The acceleration of the wind flow around the extremities of the obstacles increases the shear stress allowing enhanced deflation and wind erosion. This mechanism is further enhanced by the downflow of the two vortices developing on the lee side of the obstacle and account for the preferential deflation zones observed in the Unegt and Zuunbayan sub-basins. These high deflation and wind erosion zones form base levels for local drainage systems. The constant fluvial mobilization and transport of clastic material towards these high deflation zones locally increases the erosion rates. Cosmogenic nuclide derived surface exposure ages of rapidly eroding zones in the basin suggest that this erosion pattern was probably initiated as a consequence of the Middle Pleistocene regional increase in aridity. This conceptual model of constant interplay between fluvial mobilization of clastic material and its removal from the sink area by deflation should be considered when evaluating erosion patterns in desert areas or assessing sediment production rates at the source of large dune fields. The modifications of the wind flow pattern through time, due to erosion-related topographic changes inside the basin can also induce changes in the groundwater flows that should be taken into consideration in water management policies or when studying the various mineral deposits occurring in this type of complex basins.

Acknowledgements

This work has been financed by Orano. Field work was supported by Cogegobi who provided valuable administrative support and access to its logistics. All data relative to this work are included in the tables. We thank D. Virlogeux for field support and discussions on the regional geology. Two anonymous reviewers, A. East, P. Kapp, N.P. Mountney, Th. Pähtz, Z. Ruszkiczay-Rüdiger, Xiaoping Yang and Geomorphology Editor M. Stokes provided valuable comments to improve the initial manuscript. The ASTER AMS national facility (CEREGE, Aix-en-Provence) is supported by the INSU/CNRS, the ANR through the "Projets thématiques d'excellence" program for the "Equipements d'excellence" ASTER-CEREGE action and IRD. RB thanks G. Leduc for fruitful discussions. We declare no competing financial interest. The data used are listed in the Supplementary Tables. We would like to dedicate this manuscript to our friend and member of the ASTER Team Didier Bourlés (04/1955 – 03/2021).

References

Albritton C.C., Brooks J.E., Issawi B., Swedan A., 1990. Origin of the Qattara Depression, Egypt. Geological Society of America Bulletin, 102, 952-960.

Al-Masrahy M.A., Mountney N.P., 2015. A classification scheme for fluvial-aeolian system interaction in desert-margin settings. Aeolian Research, 17, 67-88.

Aref M.A.M., El-Khoriby E., Hamdan M.A., 2002. The role of salt weathering in the origin of the Qattara Depression, Western Desert, Egypt. Geomorphology, 45, 181-195.

Bagnold R.A., 1941. The Physics of Blown Sand and Desert Dunes. Mathuen, London.

Barchyn T.E., Hugenholtz C.H., 2013. Reactivation of supply-limited dune fields from blowouts : A conceptuel framework for state characterization. Geomorphology, 201, 172-182.

Badr T., Harion J.L., 2005. Numerical modeling of flow over stockpiles: Implications on dust emissions. Atmospheric Environment, 39, 5576-5584.

Badr T., Harion J.L., 2007. Effect of aggregate storage piles configuration on dust emissions. Atmospheric Environment, 41, 360-368.

Bassler F., 1968. Scheme for the Qattara Depression. Water Power, December 1968, 494-498.

Belnap J., Lange O.L., 2001. Central Asia Takyr. In *Biological Soil Crusts: Structure, Function, and Management*, Springer, 2001, ISBN 3-540-43757-3

Belnap J., Reynolds R.L., Reheis M.C., Phillips S.L., Urban F.E., Goldstein H.L., 2009. Sediment losses and gains across a gradient of livestock grazing and plant invasion in a cool, semi-arid grassland, Colorado Plateau, USA. Aeolian Research, 1, 27-43.

Belnap J., Munson S.M., Field J.P., 2011. Aeolian and fluvial processes in dryland regions : the need for integrated studies. Ecohydrology, 4, 615-622.

Blackwelder E., 1934. Yardangs. Geological Society of America Bulletin, 45, 159-166.

Borchers B. Marrero S., Balco G., Caffee M., Goehring B., Lifton N., Nishiizumi K., Phillips F., Schaefer J., Stone J., 2016. Geological Calibration of Spallation Production Rates. Quaternary Geochronology, 31, 188-198.

Braucher R., Merchel S., Borgomano J., Bourlès D.L., 2011. Production of cosmogenic radionuclides at great depth : A multi element approach. Earth and Planetary Science Letters, 309, 1-9.

Bullard J.E. and Livingstone I., 2002. Interactions between aeolian and fluvial systems in dryland environment. Area, 34.1, 8-16.

Bullard J.E. and McTainsh G.H., 2003. Aeolian-fluvial interactions in dryland environments : examples, concepts and Australia case study. Progress in Physical Geography, 27.4, 471-501.

Cai Maotang, Wei Mingjian, Yang Yibo, Wang Junping, Xu Dainan, 2014. Long-term cooling/drying record of North China since the middle Pleistocene from geochemical evidence of a 150 m deep drill core, Beijing plain, China. Quaternary International, 349, 419-427.

Castro I.P., Robins A.G., 1977. The flow around a surface-mounted cube in uniform and turbulent streams. Journal Fluid Mechanics, 79, 307-335.

Caves J.K., Sjostrom D.J., Mix H.T., Winnick M.J., Chamberlain C.P., 2014. Aridification of Central Asia and uplift of the Altai and Hangay Mountains, Mongolia: Stable isotope evidence. American Journal of Science, 314, 1171-1201.

Clark, P.U., Archer D., Pollard D., Blum J.D., Rial J.A., Brovkin V., Mix A.C., Pisias N.G., Roy M., 2006. The middle Pleistocene transition: characteristics, mechanisms, and implications for long-term changes in atmospheric pCO2. Quaternary Science Reviews, 25, 3150–3184.

Courrech du Pont, S., Narteau C., Gao Xin, 2014. Two modes for dune orientation. Geology, 42.9, 743–746.

Crosby B.T., and Whipple K.X., 2006. Knickpoint initiation and distribution within fluvial networks: 236 waterfalls in the Waipaoa River, North Island, New Zealand. Geomorphology, 82, 16-38.

Currie, P.J., and Eberth, D.A., 1993. Palaeontology, sedimentology and palaeoecology of the Iren Dabasu Formation (Upper Cretaceous), Inner Mongolia, People's Republic of China. Cretaceous Research, 14, 127-144.

Daoudene Y., Gapais D., Cogné J-P., Ruffet G., 2017. Late Jurassic – Early Cretaceous continental extension in northeast Asia – Relationships to plate kinematics. Bulletin de la Société Géologique de France, 188, 10.

Dee, D., et al. (2011), The ERA-Interim reanalysis: Configuration and performance of the data assimilation system, Quaterly Journal of the Royal Meteorological Society, 137 (656), 553–597.

Dill H.G., Khishigsuren S., Majigsuren Yo., Myagmarsuren S., Bulgamaa J., 2006. Geomorphological studies along a transect from the taiga to the desert in Central Mongolia – Evolution of landforms in the mid-latitude continental interior as a function of climate and vegetation. Journal of Asian Earth Sciences, 27, 241-264.

Draut A.E., 2012. Effects of river regulation on aeolian landscapes, Colorado River, southwestern USA. Journal of Geophysical Research, 117, F02022, doi:10.1029/2011JF002329.

Ehsani A.H., and Quiel F., 2008. Application of Self Organizing Map and SRTM data to characterize yardangs in the Lut desert, Iran. Remote Sensing of Environment, 112, 3284-3294.

Furieri B., Russeil S., Harion J.L., Turpin C., Santos J.M., 2012. Experimental surface flow visualization and numerical investigation of flow structure around an oblong stockpile. Environmental Fluid Mechanics, 12, 533-553.

Gao Xin, Narteau C., Rozier O., 2015, Development and steady states of transverse dunes : A numerical analysis of dune pattern coarsening and giant dunes. Journal of Geophysical Research : Earth Surface, 120, 2200-2219.

Goudie A.S., 1989. Wind erosion in deserts. Proceedings of the Geological Association, 100, 83-92

Goudie A.S., 1991. Pans. Progress in Physical Geography, 15, 3, 221-237.

Goudie A.S. and Wells G.L., 1995. The nature, distribution and formation of pans in arid zones. Earth-Science Reviews, 38, 1-69

Graham, S.A., Hendrix, M S., Johnson, C.L., Badamgarav, D., Badarch, G., Amory, J., Porter, M., Barsbold, R., Webb, L.E., Hacker, B.R., 2001. Sedimentary record and tectonic implications of late Mesozoic rifting, southeast Mongolia. Geological Society of America Bulletin, 113, 1560-1579.

Granger D. E., and Muzikar P. F., 2001. Dating sediment burial with in situ-produced cosmogenic nuclides: theory, techniques, and limitations. Earth and Planetary Science Letters, 188, 269–281.

Granger D.E., 2006. A review of burial dating methods using 26Al and 10Be. In *In situ-produced cosmogenic nuclides and quantification of geological processes* (Eds. Siame, L., Bourlès, D.L., and Brown, E.T.). Geological Society of America Special Paper, 415, 1-16.

Grizard P., 2017. Fonctionnement hydrogéologique et hydrochimique du bassin crétacé de Tsagaan Els (Dornogobi, Mongolie). PhD, Paris Science and Lettres Research University, 350 p.

Grizard P., Schmitt J-M., Goblet P., 2019. Hydrogeology of an arid endorheic basin (Tsagaan Els, Dornogobi, Mongolia) : field data and conceptualization, three-dimensional groundwater modeling, and water budget. Hydrogeology Journal, doi.org/10.1007/s10040-018-1868-1

Han Wenxia, Fang Xiaomin, Berger A., 2012. Tibet forcing of mid-Pleistocene synchronous enhancement of East Asian winter and summer monsoons revealed by Chinese loess record. Quaternary Research, 78, 174-184.

Heermance R. V., Pullen A., Kapp P., Garzione C. N., Bogue S., Ding L., Song P., 2013. Climatic and tectonic controls on sedimentation and erosion during the Pliocene-Quaternary in the Qaidam Basin (China). Geological Society of America Bulletin, 125, 833–856.

Hesp P., 2002. Foredunes and blowouts : initiation, geomorphology and dynamics. Geomorphology, 48, 245-268

Hipondaka M.H.T., 2005. The development and Evolution of Etosha Pan, Namibia. PhD thesis, University Würzburg, 152 p.

Hunt J.C.R., Abell C.J., Peterka J.A., Woo H., 1978. Kinematical studies of the flows around free or surface-mounted obstacles ; applying topology to flow visualization. Journal of Fluid Mechanisc, 86.1, 179-200.

Iversen J.D., Wang Wen-Ping, Rasmussen K.R., Mikkelsen H.E., Hasiuk J.F., Leach R.N., 1990. The effect of a roughness element on local saltation transport. Journal of Wind Engineering and Industrial Aerodynamics, 36, 845-854.

Jackson D.W.T., Beyers M., Delgado-Fernandez I., Baas A.C.W., Cooper A.J., Lynch K., 2013. Airflow reversal and alternating corkscrew vortices in foredune wake zones during perpendicular and oblique offshore winds. Geomorphology, 187, 86-93.

Johnson C.L., 2004. Polyphase evolution of the East Gobi basin : sedimentary and structural records of Mesozoic-Cenozoic intraplate deformation in Mongolia. Basin Research, 16, 79-99.

Johnson, C.L.,Webb, L.E., Graham, S.A., Hendrix, M.A. & Badarch, G., 2001. Sedimentary and structural records of late Mesozoic high-strain extension and strain partitioning, East Gobi basin, southern Mongolia. Geological Society of America Bulletin, 194, 413-434.

Jolivet M., Ritz J-F., Vassallo R.,Larroque C., Braucher R., Todbileg M., Chauvet A., Sue C., Arnaud N., De Vicente R., Arzhanikova A., Arzhanikov S., 2007. The Mongolian summits: An uplifted, flat, old but still preserved erosion surface. Geology, 35.10, 871-874.

Kapp P., Pelletier J.D., Rohrmann A., Heermance R., Russel J., Ding L., 2011. Wind erosion in the Qaidam basin, central Asia : Implications for tectonics, paleoclimate, and the source of the Loess Plateau. GSA Today, 21.4/5, https://doi.org/10.1130/GSATG99A.1

Kapp P., Pullen A., Pelletier J.D., Russell J., Goodman P., Cai F., 2015. From dust to dust : Quaternary wind erosion of the Mu Us Desert and Loess Plateau, China. Geology, 43, 835-838, doi:10.1130/G36724.1

Krapf C.B.E., Stollhofen H., Stanistreet I.G., 2003. Contrasting styles of ephemeral river systems and their interaction with dunes of the Skeleton Coast erg (Namibia). Quaternary International, 104, 41-52.

Laity J.E., 1987. Topographic effects on ventifact development, Mojave Desert, California. Physical Geography, 8, 113-132.

Laity J., 2003. Aeolian destabilization along the Mojave River, Mojave Desert, California : Linkages among fluvial, groundwater, and aeolian systems. Physical Geography, 24.3, 196-221, https://doi.org/10.2747/0272-3646.24.3.196

Laity J.E., 2011. Wind erosion in drylands. In Thomas D.S.G. (Ed), *Arid Zone Geomorphology. Process, Form and Change in Drylands*. Wiley & Sons, UK.

Lamb, M.A., Hanson, A.D., Graham, S.A., Badarch, G., Webb, L.E., 1999. Left- lateral sense offset of upper Proterozoic to Paleozoic features across the Gobi Onon, Tost, and Zuunbayan faults in southern Mongolia and implications for other Central Asian faults. Earth and Planetary Science Letters, 173, 183–194.

Lisle T.E. and Hilton S., 1992. The volume of fine sediment in pools: An index of sediment supply in gravel-bed streams. Water Resources Bulletin, 28, 371–383.

Liu Baoli and Coulthard T.J., 2015. Mapping the interactions between rivers and sand dunes: Implications for fluvial and aeolian geomorphology. Geomorphology, 231, 246-257.

Liu Baoli and Coulthard T.J., 2017. Modelling the interaction of aeolian and fluvial processes with a combined cellular model of sand dunes and river systems. Computers & Geosciences, 106, 1-9.

Liu Zhenqing, Diao Zheng, Ishihara T., 2019. Study of the flow fields over simplified topographies with different roughness conditions using large eddy simulations. Renewable Energy, 136, 968-992.

Maroulis J.C., Nanson G.C., Price D.M., Pietsch T., 2007. Aeolian-fluvial interaction and climate change: source-bordering dune development over the past ~100 ka on Cooper Creek, central Australia. Quaternary Science Reviews, 26, 386-404.

McMillan M. and Schoenbohm L.M., 2020. Large-scale Cenozoic wind erosion in the Puna Plateau : The Salina del Fraile Depression. Journal of Geophysical Research – Earth Surface, 125, e2020JF005682, https://doi.org/10.1029/2020JF005682.

Middleton N.J., 1991. Dust storms in the Mongolian People's Republic. Journal of Arid Environments, 20, 287-297.

Miller R.McG., Pickford M., Senut B., 2010. The geology, palaeontology and evolution of the Etosha Pan, Namibia : Implications for terminal Kalahari deposition. South African Journal of Geology, 113.3, 307-344.

Mountney N.P., 2006. Eolian facies models. In Posamentier H.W. and Walker R.G. (Eds), *Facies models revisited*, SEPM special publication, Tulsa, Oklahoma, USA, 84, 19-83.

Mountney N.P., Russell A.J., 2009. Aeolian dune-field development in a water table-controlled system: Skeiđarársandur, Southern Iceland. Sedimentology, 56, 2107-2131.

Muhs D.R., Stafford T.W., Cowherd S.D., Mahan S.A., Kihl R., Maat P.B., Bush C.A., Nehring J., 1996. Origin of the late Quaternary dune firlds of northeastern Colorado. Geomorphology, 17, 129-149.

Muhs D.R., Reynolds R.L., Been J., Skipp G., 2003. Eolian sand transport pathways in the southwestern United States : importance of the Colorado River and local sources. Quaternary International, 104, 3-13.

Natsagdorj L., Jugder D., Chung Y.S., 2003. Analysis of dust storms observed in Mongolia during 1937 – 1999. Atmospheric Environment, 37, 1401-1411.

Naugolnykh S.V., 2016. Upper Cretaceous Paleosols of the Bain-Dzak Section, Southern Mongolia. Paleontological Journal, 50.12, 1451-1469.

Pelletier J.D., 2006. Sensitivity of playa windblown-dust emission to climatic and anthropogenic change. Journal of Arid Environments, 66, 62-75.

Powell D.M., 2009. Dryland Rivers : Processes and Forms. In Parsons A.J. and Abrahams A.D. (Eds), *Geomorphology of the Desert Environments*. Second Edition, Spinger Science+Business Media.

Pullen A., Kapp P., Chen N., 2018. Development of stratigraphically controlled, eolian-modified unconsolidated gravel surfaces and yardang fields in the wind-eroded Hami Basin, northwestern China. Geological Society of America Bulletin, 130.3/4, 630-648, https://doi.org/10.1130/B31734.1

Reheis M .C., 1997. Dust deposition downwind of Owens (dry) Lake, 1991-1994 : Preliminary findings. Journal of Geophysical Research, 102.D22, 25999-26008.

Reheis M.C., 2006. A 16-year record of aeolian dust in Southern Nevada and California, USA : Controls on dust generation and accumulation. Journbal of Arid Environments, 67, 487-520.

Reheis M.C. and Kihl R., 1995. Dust deposition in southern Nevada and California, 1984-1989 : Relations to climate, source area, and source lithology. Journal of Geophysical Research, 100.D5, 8893-8918.

Reheis M.C. and Urban F.E., 2011. Regional and climatic controls on seasonal dust deposition in the southwestern U.S. Aeolian Research, 3, 3-21.

Reynolds R.L., Yount J.C., Reheis M., Goldstein H., Chaver (Jr.) P., Fulton R., Whitney J., Fuller C., Forester R., 2007. Dust emission from wet and dry playas in the Mojave Desert, USA. Earth Surface Processes and Landforms, 32, 1811-1827.

Rixhon G., Braucher R., Bourlès D., Siame L., Bovy B., Demoulin A. Quaternary river incision in NE Ardennes (Belgium) - Insights from 10Be/26Al dating of river terraces. Quaternary Geochronology 6 (2011) 273-284

Rohrmann A., Heermance R., Kapp P., Cai Fulong, 2013. Wind as the primary driver of erosion in the Qaidam Basin, China. Earth and Planetary Science Letters, 374, 1-10.

Rosen M.R., 1994. The importance of groundwater in playas : a review of playa classification and the sedimentology and hydrology of playas. In *Paleoclimate and Basin Evolution of Playa Systems*, Geological Society of America Special Paper 289, Rosen M.R. (ed.). Boulder, Colorado, USA, 1-18.

Ruszkiczay-Rüdiger Z., Fodor L.I., Horváth E., 2007. Neotectonics and Quaternary lansdcape evolution of the Gödöllő Hills, Central Pannonian Basin, Hungary. Global and Planetary Change, 58, 181-196.

Ruszkiczay-Rüdiger Z., Fodor L., Horváth E., Telbisz T., 2009. Discrimination of fluvial, aeolian and neotectonic features in a low hilly landscape: A DEM-based morphotectonic analysis in the Central Pannonian Basin, Hungary. Geomorphology, 104, 203-217.

Ruszkiczay-Rüdiger Z., Braucher R., Csillag G., Fodor L.I., Dunai T.J., Bada G., Bourlès D., Müller P., 2011. Dating Pleistocene aeolian landforms in Hungary, Central Europe, using in situ produced cosmogenic ^{10}Be. Quaternary Geochronology, 6, 515-529.

Sankey J.B., Kasprak A., Caster J., East A.E., Fairley H.C., 2018a. The response of source-bordering aeolian dunefields to sediment-supply changes 1 : Effects of wind variability and river-valley morphodynamics. Aeolian Research, 32, 228-245.

Sankey J.B., Caster J., Kasprak A., East A.E., 2018b. The response of source-bordering aeolian dunefields to sediment-supply changes 2 : Controlled floods of the Colorado River in Grand Canyon, Arizona, USA. Aeolian Research, 32, 154-169.

Santos M.G.M., Hartley A.J., Mountney N.P., Peakall J., Owen A., Merino E.R., Assine M.L., 2019. Meandering rivers in modern desert basins: Implications for channel planform controls and prevegetation rivers. Sedimentary Geology, 385, 1-14

Sebe K., Csillag G., Ruszkiczay-Rüdiger Z., Fodor L., Thamó-Bozsó E., Müller P., Braucher R., 2011. Wind erosion under cold climate: A Pleistocene periglacial mega-yardang system in Central Europe (Western Pannonian Basin, Hungary). Geomorphology, 134, 470-482.

Siame L., Bellier O., Braucher R., Sébrier M., Cushing M., Bourlès D.L., Hamelin B, Baroux E., de Voogd B., Raisbeck G., Yiou F. 2004. Local erosion rates versus active tectonics: Cosmic ray exposure modelling in Provence (South-East France), Earth and Planetary Science Letters, 220, 345-364.

Simmons, A., Uppala S., Dee D., Kobayashi S., 2007. ERA-interim: New ECMWF reanalysis products from 1989 onwards. ECMWF Newsletter, 110, 25–35.

Smith W.H.F., and Wessel P., 1990. Gridding with continuous curvature splines in tension. Geophysics, 55, 293-305.

Smyth T.A.G., 2016. A review of Computational Fluid Dynamics (CFD) airflow modelling over aeolian landforms. Aeolian Research, 22, 153-164.

Stone, J. O. , 2000. Air pressure and cosmogenic isotope production. Journal of Geophysical Research, 105 (B10), 23753–23759.

Sun, Y., Yin, Q., Crucifix, M, Clemens S. C., Araya-Melo P., Liu W., Qiang X., Liu Q., Zhao H., Liang L., Chen H., Li Y., Zhang L, Dong G., Li, . Zhou W., Berger A., An Z. 2019. Diverse manifestations of the mid-Pleistocene climate transition. Nature Communication, 10, 352.

Tominaga Y., Okaze T., Mochida A., 2018. Wind tunnel experiment and CFD analysis of sand erosion/deposition due to wind around an obstacle. Journal of Wind Engineering & Industrial Aerodynamics, 182, 262-271.

Turpin C., Harion J.L., 2010. Effects of the topography of an industrial site on dust emissions from open storage yards. Environmental Fluid Mechanics, 10, 677-690.

Vassallo R., M. Jolivet, J-F Ritz, R. Braucher, Ch. Larroque, C. Sue, M. Todbileg, D. Javkhlanbold, 2007. Uplift age and rates of the Gurvan Bogd system (Gobi-Altay) by apatite fission track analysis. Earth Planetary Sciences Letter, 259, 333-346.

Vermeesch, P. (2007), CosmoCalc: An Excel add- in for cosmogenic nuclide calculations, *Geochem. Geophys. Geosyst.*, 8, Q08003, doi:10.1029/2006GC001530.

Vermeesch, P., 2012. On the visualisation of detrital age distributions. Chemical Geology, 312-313, 190-194, doi: 10.1016/j.chemgeo.2012.04.021 0

Wakes S.J., Maegli T., Dickinson K.J., Hilton M.J., 2010. Numerical modelling of wind flow over a complex topography. Environmental Modeling & Software, 25, 237-247.

Wang Jida, Song Chunqiao, Reager J.T., Yao Fangfang, Famiglietti J.S., Sheng Yongwei, MacDonald G.M., Brun F., Müller Schmied H., Marston R.A., Wada Y., 2018. Recent global decline in endorheic basin water storage. Nature Geoscience, 11, 926-932.

Wang Wanfu, Dong Zhibao, Wang Tao, Zhang Guobin, 2006. The equilibrium gravel coverage of the deflated gobi above the Mogao Grottoes of Dunhuang, China. Environmental Geology, 50, 1077-1083.

Wang Xin, Dettman D.L., Wang Mi, Zhang Jinhui, Saito Y., Quade J., Feng Song, Liu Jianbao, Chen Fahu, 2020. Seasonal wet-dry variability of the Asian monsoon since the middle Pleistocene. Quaternary Science Reviews, 247, 106568.

Webb L.E., Johnson C.L., 2006. Tertiary strike-slip faulting in southeastern Mongolia and implications for Asian tectonics. Earth and Planetary Science Letters, 241, 323-335.

Wessel P., and Smith W.H.F., 1991. Free software helps map and display data. EOS Transactions American Geophysical Union, 72, 441, 445-446.

Wiggs G.F.S., Livingstone I., Warren A., 1996. The role of streamline curvature in sand dune dynamics: evidence from field and wind tunnel measurements. Geomorphology, 17, 29-46.

Williams G.E., 1968. Formation of large-scale trough cross-stratification in a fluvial environment. Journal of Sedimentary Petrology, 38(1), 136-140.

Williams M., 2015. Interactions between fluvial and aeolian geomorphic systems and processes: Examples from the Sahara and Australia. Catena, 134, 4-13.

Whipple K.X., and Tucker G.E., 1999. Dynamics of the stream-power river incision model: Implications for heigh limits of mountain ranges, landscape response timescales, and research needs. Journal of Geophysical Research, 104.B8, 17661-17674.

Wolfe S.A. and Nickling W.G., 1993. The protective rôle of sparse vegetation in wind erosion. Progress in Physical Geography, 17, 50-68.

Wolkowinsky A.J. and Granger D. E.,2004. Early Pleistocene incision of the San Juan River, Utah, dated with 26Al and 10Be Geology, 32 (9), 749–752.

Wormald R.J., Eckardt F.D., Vearncombe J. and S., 2003. Spatial Distribution Analysis of Pans in Botswana : The Importance of Structural Control. South African Journal of Geology, 106, 287-290.

Yapiyev V., Sagintayev Zh., Inglezakis V.J., Samarkhanov K., Verhoef A., 2017. Essentials of endorheic basins and lakes: A review in the context of current and future water ressource management and mitigation activities in Central Asia. Water, 9, 798; doi:10.3390/w9100798.

Yao Z.Y., Wang T., Han Z.W., Zhang W.M., Zhao A.G., 2007. Migration of sand dunes on the northern Alxa Plateau, Inner Mongolia, China. Journal of Arid Environments, 70, 80-93.

Figure captions

Figure 1: A: Large scale satellite image (Google Earth®, Landsat Images, Copernicus) showing the Tsagaan Els depression and surrounding basement ridges with indication of the major faults (Graham et al., 2001). The dotted lines represent the 750 m altitude contour line that highlights the lowest parts of the depression. B: 1 arc second resolution Shuttle Radar Topography Mission (SRTM1) Digital Elevation Model (DEM) documenting the topography of the Tsagaan Els depression. The red and blue lines correspond to the track of the topographic profiles shown at the bottom of the figure. The DEM and profiles were drawn using the GMT Software (Smith and Wessel, 1990). On profiles 1 and 2, the thick colored line represent the mean altitude of a staked series of individual profiles sampled every km over 5 km on each sides of the indicated profile track. The grey envelope indicates the altitude dispersal. Note that vertical exaggeration is x 20. Data were acquired every 20 m from the SRTM1 DEM.

Figure 2: Geological map of the Tavan Har structure and its surroundings (modified from Grizard, 2017). Piezometric lines represent the aquifer in the Late Cretaceous Upper Sainshand Formation (K2Ss2) and have been simplified from Grizard et al. (2019). BB: Baruun Bayan spring; DB: Dund Bayan spring. BP: Bayanshire Plateau (the limits of the plateau are indicated by a dotted line). Arrows on faults indicate sense of movement.

Figure 3: Field photographs of the Tavan Har structure (see Figure 2 for location): a) view from the NE of the Tavan Har basement high and the conical structure (labelled morphological cone) to the north. Note the flat summit of the basement high. The distance scale applies to the background. b) the Cretaceous series cropping out in the conical structure are tilted and clearly not parallel to the morphological surface. The white dashed lines indicate bedding. c) views of the southern edge of the basement high, showing the morphological scarp corresponding to the differential erosion along the Cretaceous normal faults. Only the Lower Cretaceous series are exposed. d) view of the summit plateau on the basement high. The surface covered with sand (background) is separated from the sand-free foreground by a small canyon incised in the basement. e) aeolian deposits and thin gravel layer on the conical structure. These are the only sediments deposited on that surface and do not correspond to an alluvial fan. f) Colluvium on the metamorphic basement. These deposits are formed by largely in-situ produced unsorted and sharp-edged basement-rock fragments. The camera lens cover is 5 cm in diameter.

Figure 4: Simplified geological and tectonic map of the Tsagaan Els depression. Only the largest dune fields and sand sheets are shown; the rest of the surface is largely free of sand and covered by desert pavements of gravel. Similar to Figure 1, the 750 m contour line highlights the lowest depressions in the basin. Erosion rates calculated from cosmogenic ^{10}Be and ^{26}Al concentrations measured in surface samples are indicated as color-coded rectangles. See Supplementary Tables 1 and 2 for details on results from cosmogenic nuclides analysis.

Figure 5: Satellite and field photographs of aeolian features in the Tsagaan Els depression. a) Satellite images (Google Earth® CNES/Airbus 2021 and Maxar Technologies 2021) of the large dune fields east of the Zuunbayan sub-basin (Figures 1 and 4) showing parabolic and transverse dunes. b) Satellite images (Google Earth® Maxar Technologies 2021) and field photograph of longitudinal dunes developing immediately south of an ephemeral lake north of the Tavan Har conical structure. c) Field view of a reg-type landscape on which only the vegetation allows sand accumulation. To the right, small-scale sand shadow behind a bush. Such accumulations can be up to several meters in length and about 1 meter in height (coppice dunes). The dotted line white arrows indicate the sand motion direction for each image.

Figure 6: Meteorological data from the Sainshand (left) and Bayandobosuma (right) weather stations (Figure 1) as recorded in the Climate Data Online catalog of the U.S. National Oceanic and Atmospheric Administration. The bottom right diagram shows the compilation of storm conditions (wind speed over 30 $m.s^{-1}$) for the Sainshand station. N represents the number of data for each diagram. The small "+" characters on the temperature diagrams and the starts on the precipitation diagrams indicate the outliers.

Figure 7: Examples of wind pattern obtained using the ERA-Interim reanalysis data. The three models to the left correspond to monthly averages. Note the formation of the large vortices on the lee side of the Tavan Har massif as well as the contrast in wind velocity between the Unegt and Zunnbayan basins. The three models to the right correspond to stormy days (wind speed over 30 $m.s^{-1}$).

Figure 8: Interpolated sand motion map for the whole Tsagaan Els depression (a) and specifically for the Tavan Har structure (b). The black arrows indicate the direction of sand displacement (no velocity or rate indicated; color scale in degrees from north). The vectors associated with yellow dots were obtained from dunes and those associated with red dots from the mean direction measure on at least 20 sand shadow structures localized within a 100 m radius. The interpolation was performed using the "surface" calculation routine of the GMT Software (Smith and Wessel, 1990).

Note that the density of data is largely controlled by the occurrence of sand in the various regions of the basin which has a direct influence on the confidence level of the interpolation.

Figure 9: a: erosion rates calculated for each surface sample following calculation options 1 or 2. See text for details on the calculation hypothesis. b: kernel density plot of best fit erosion rates for the surface samples (n is the number of erosion values considered for the calculation. See top figure for the references of the corresponding samples).

Figure 10: Comparison between erosion rates obtained from cobbles and from amalgams for the double samples. Note the 7 samples individualized by their name and having a significant difference between the erosion rate calculated on amalgam and the one calculated on cobble. See text for explanation.

Figure 11: a) Geology and topography of the Bayanshire plateau and the western part of the main depression zone. The plateau presents two surfaces, the upper one to the north being separated from the lower one by the North Zuunbayan fault trace. The main depression is mostly filled with playas supporting ephemeral lakes. b) View from the south of the southern scarp of the Bayanshire plateau. The Cretaceous strata are exposed up to the last meter before the top suggesting that the Cenozoic strata are very thin. The scarp is about 20 m high. c) View from the SW of the lower surface of the Bayanshire plateau. The cars in the circle give the scale. d) Sediment log of the three profiles (see text for a complete description).

Figure 12: ^{10}Be and ^{26}Al concentrations and ^{26}Al/^{10}Be ratios versus depth in the three sampled pits. Black dots are samples from the lithified lower sedimentary unit, triangles are surface samples and dots are samples coming from a more sandy layer (so called “active” layer) on top of the indurated unit and below the surface layer composed of small pebbles. Dashed line is the best fit model obtained for the lithified unit (black dots).

Figure 13: Following Siame et al (2004) and Wolkowinsky and Granger (2004), these contour plots aim at determining the uncertainties associated to the erosion and exposure ages. Black dots are the minimum χ^2 corresponding to the best erosion and exposure age estimates. Black arrows point to either maximum or minimum erosion rates (vertical) or exposure ages (horizontal) associated to those best estimates. These uncertainties are determined using the minimum χ^2 value plus one (Wolkowinsky and Granger, 2004).

Figure 14: Model of wind flow and wind erosion patterns around the Tavan Har massif. The frontal depression corresponds to an area combining a maximum velocity of the wind flow arriving into the Unegt Basin and retrograding erosion from the two ends of the Tavan Har massif. The strong

acceleration of the wind flow around the extremities of the massif associated to the down-flow of the vortices developing in the lee zone increases the shear stress and generates strong erosion in the secondary depressions. The grey areas mark the position of the low velocity zones behind the Mandakh-Saykhandulaan ridge and the Tavan Har massif. Cross sections are showing the lithology of the substratum as well as the wind flow pattern.

Figure 15: Evolution of the $^{26}Al/^{10}Be$ at a given depth after a shift of erosion from 3 to 10 m/Ma. Values near the dots are the time span (exposure time at surface) since the shift. In that peculiar case, it takes more than 10 Ma to reach the new equilibrium state. An “apparent” burial age up to 1 Ma can be determined.

Figure 1

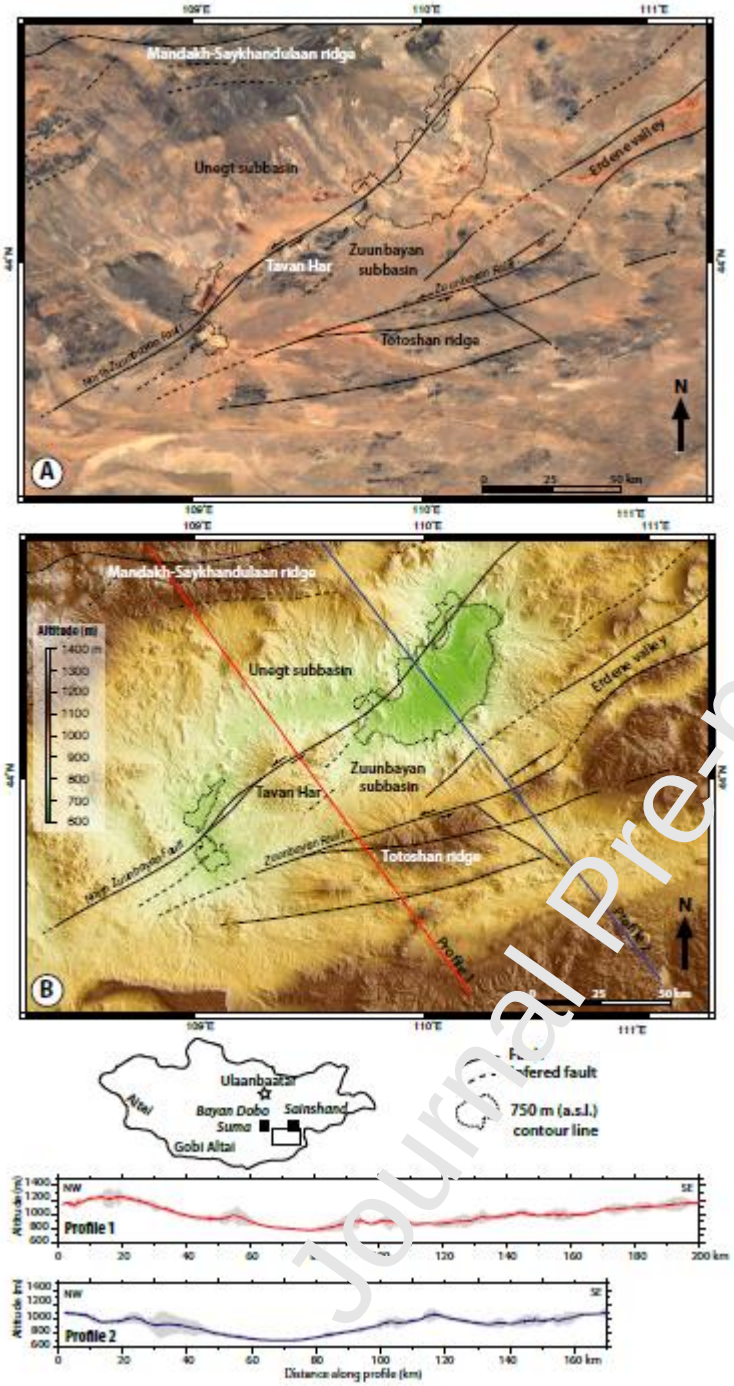

Figure 2

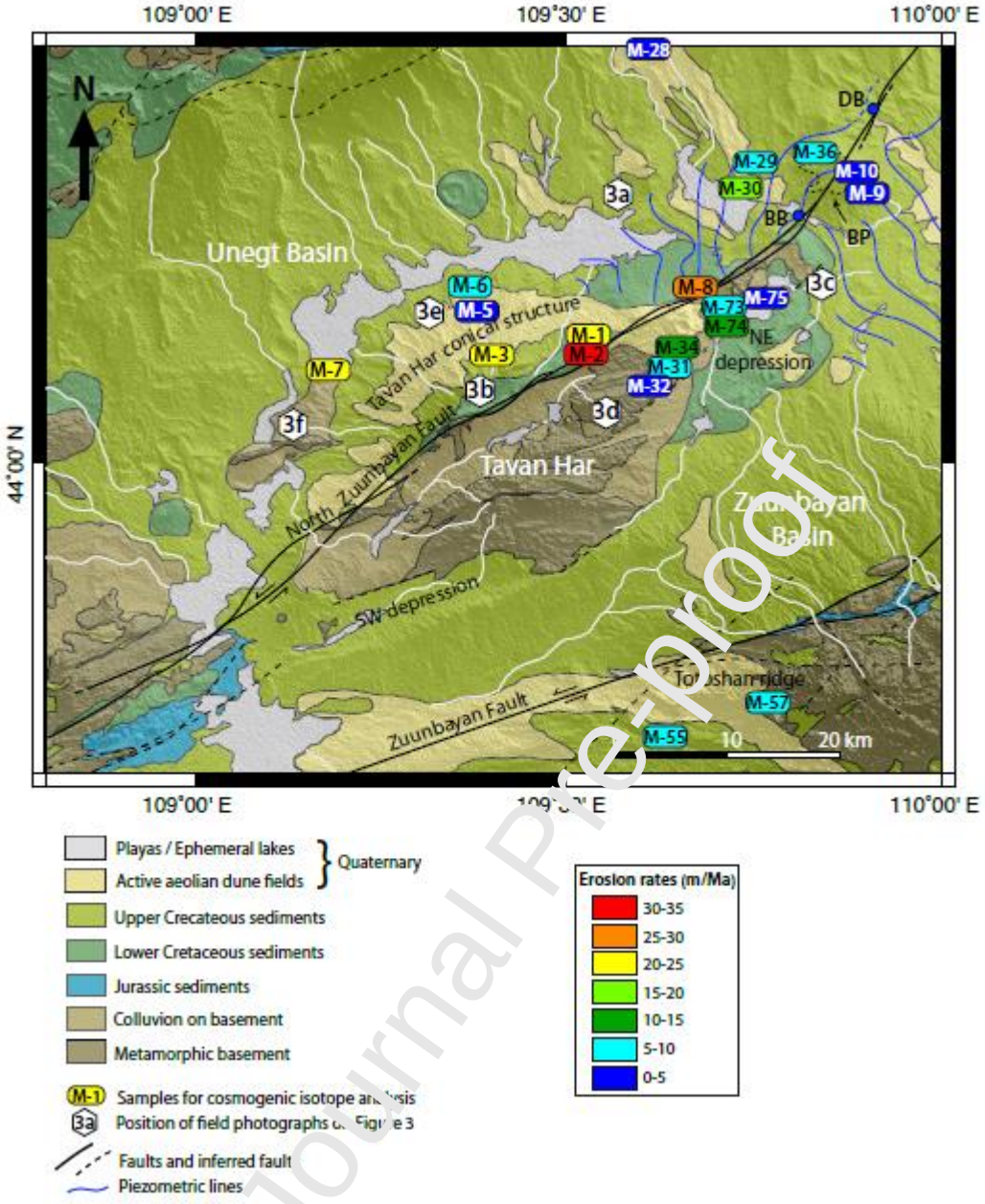

Figure 3

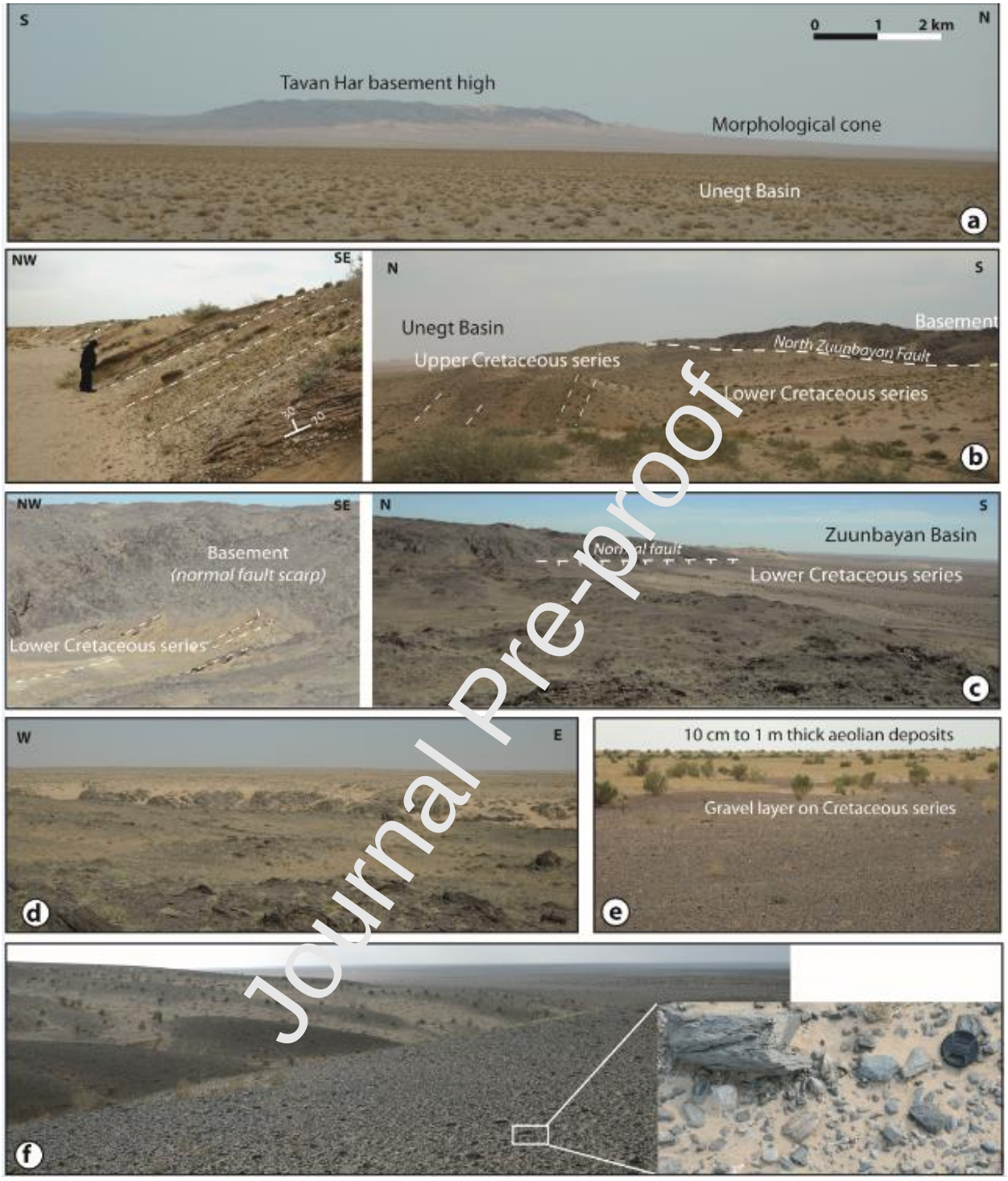

Figure 4

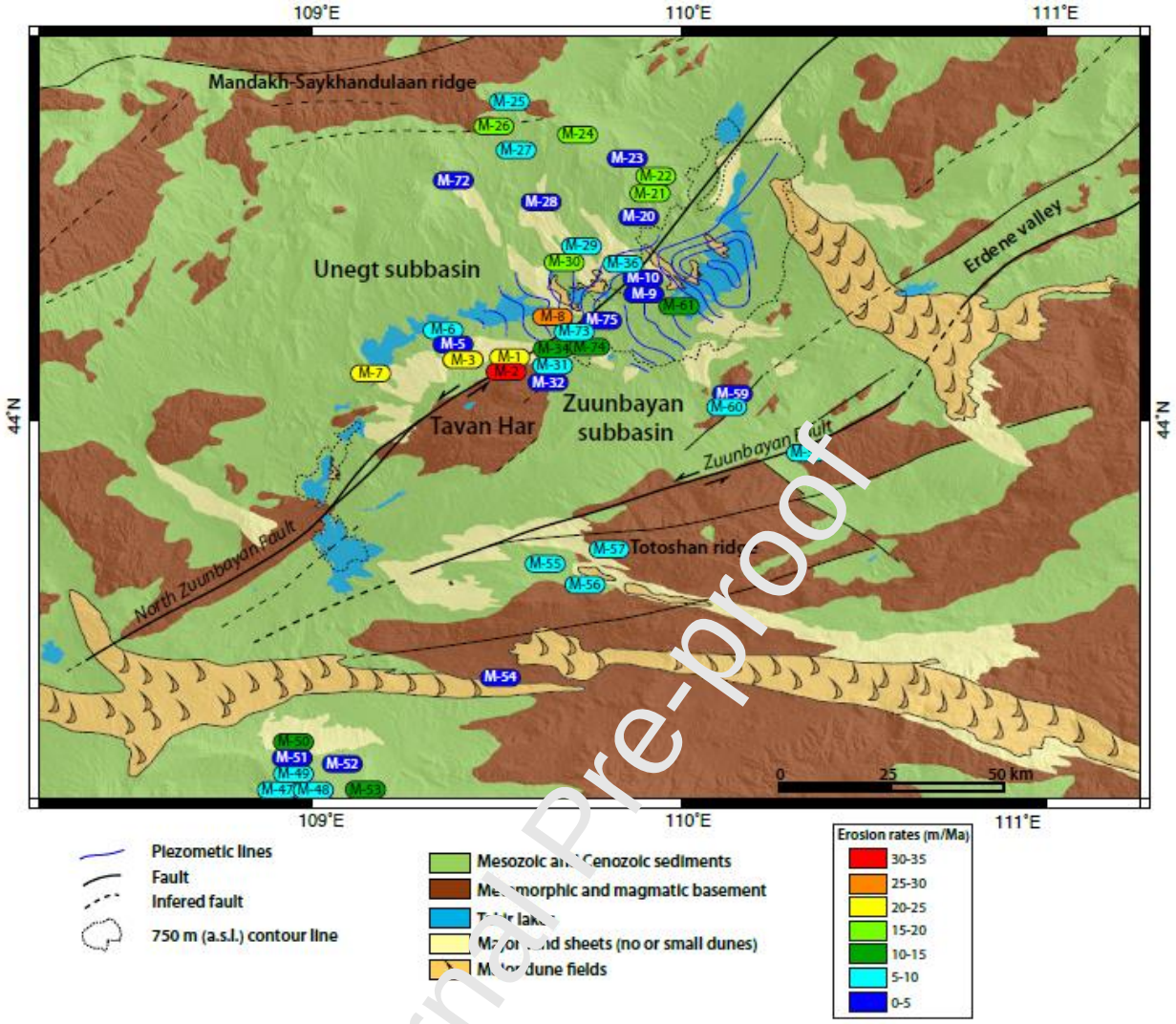

Figure 5

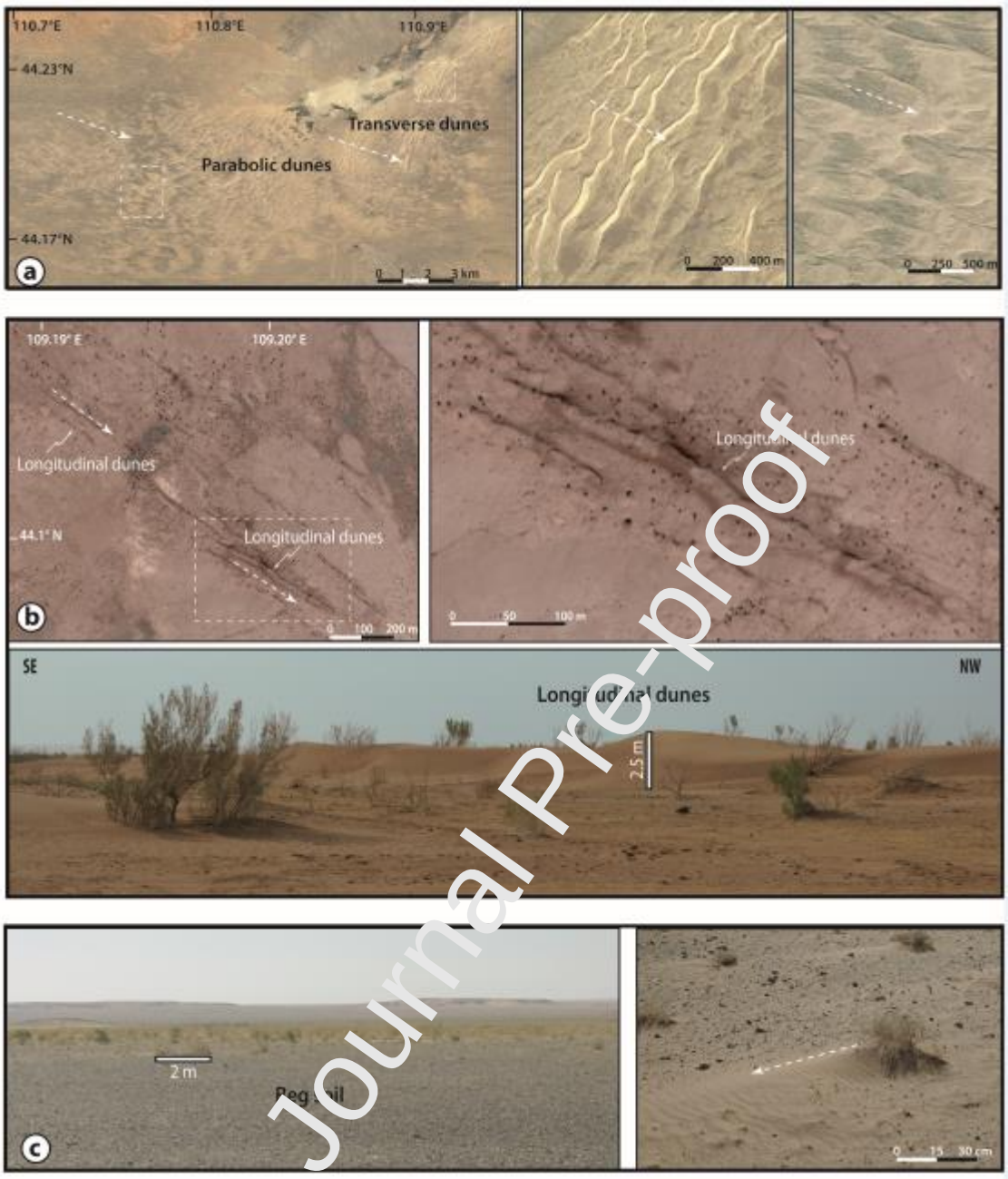

Figure 6

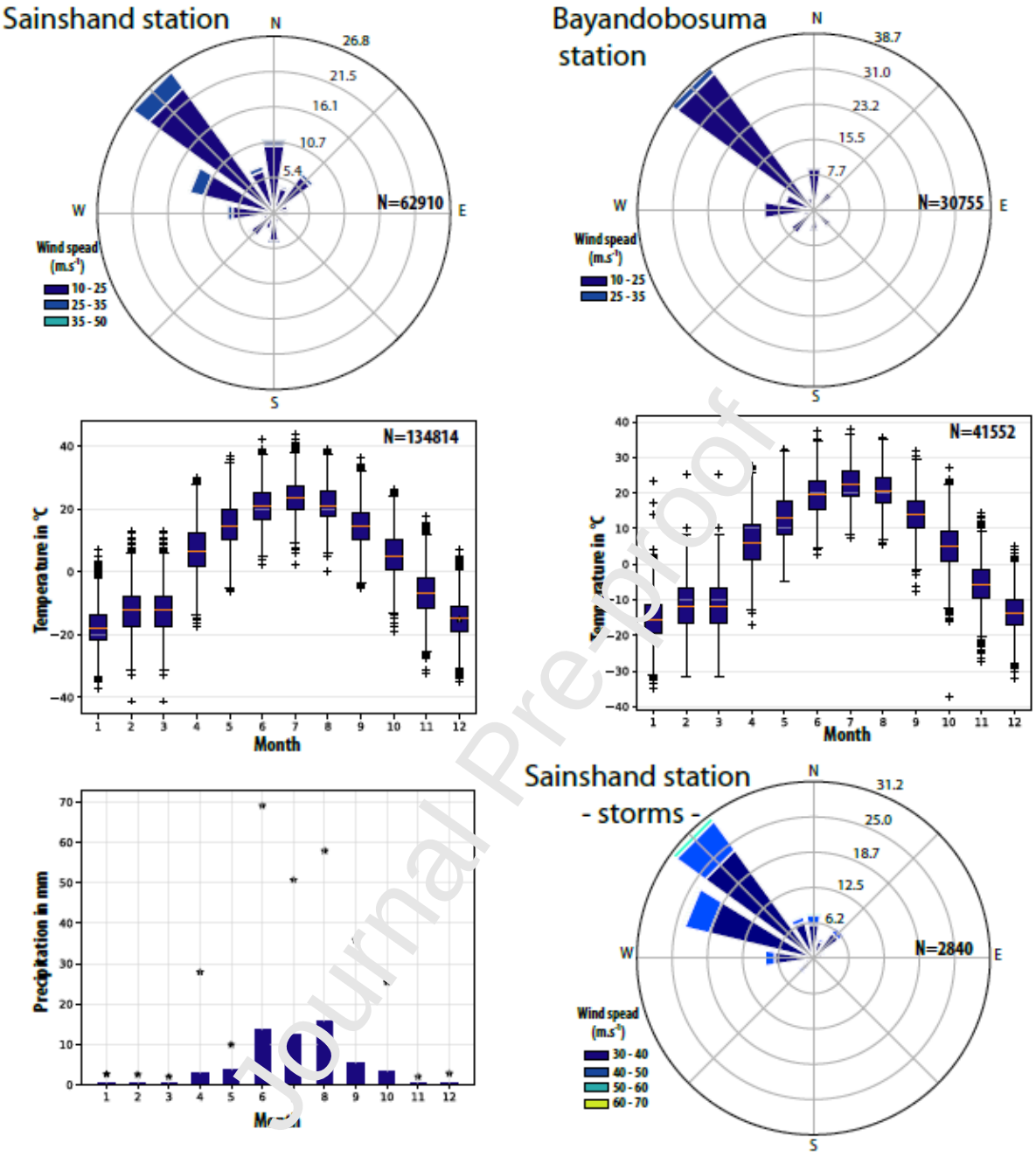

Figure 7

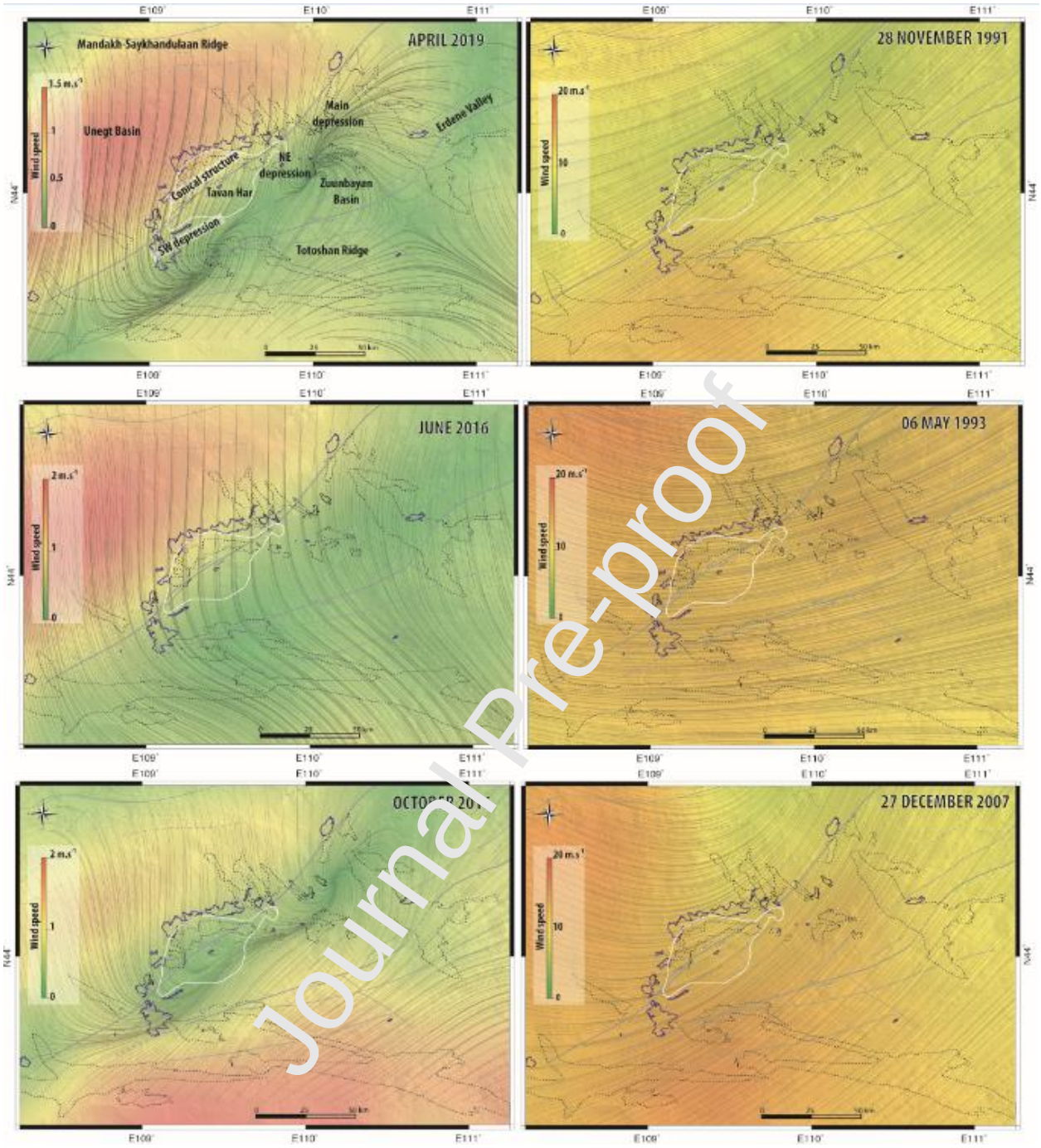

Figure 8

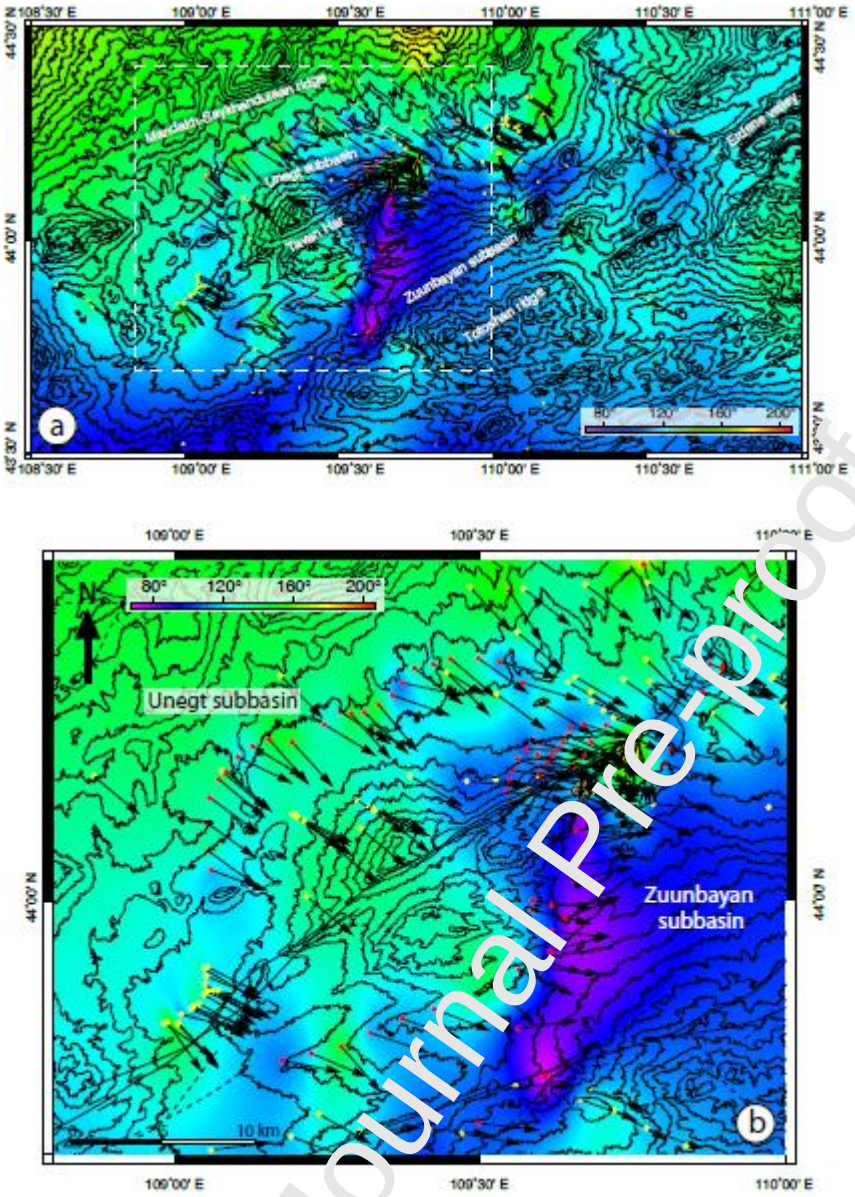

Figure 9

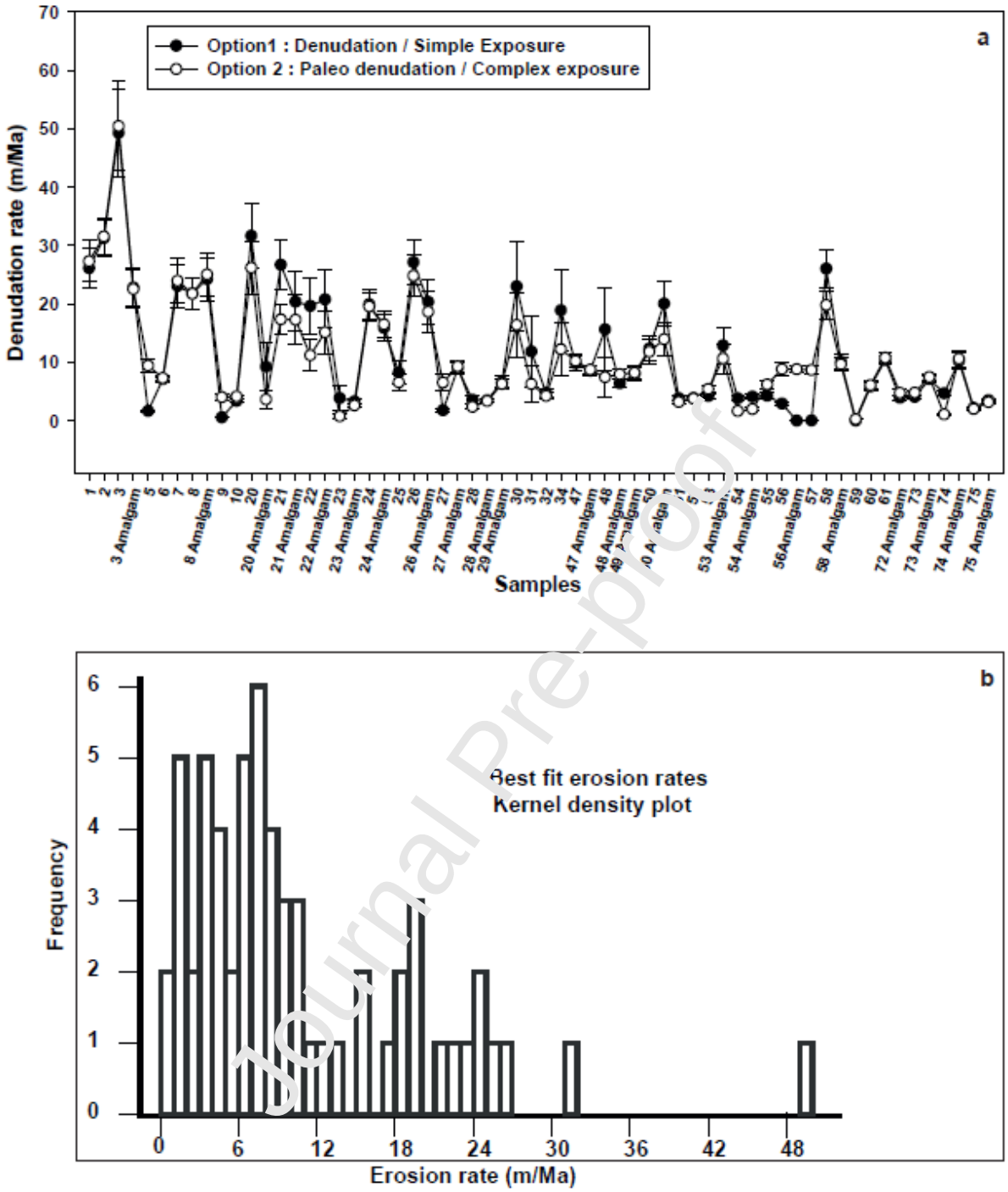

Figure 10

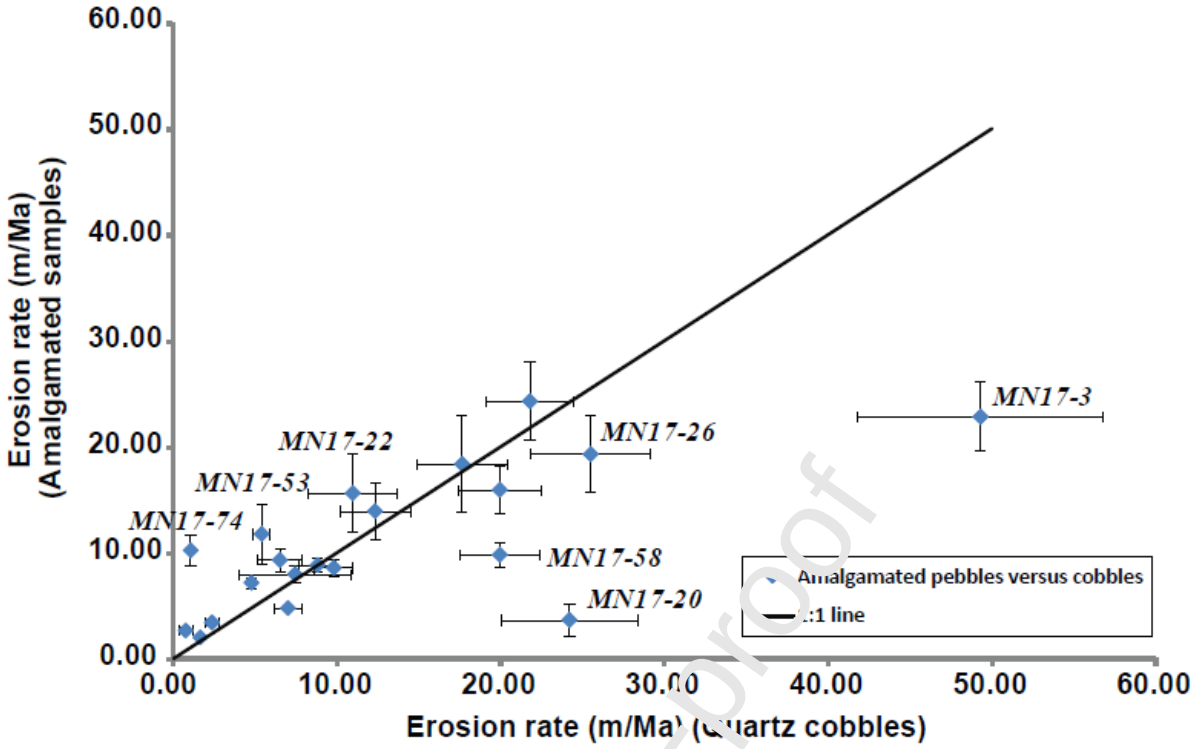

Figure 11

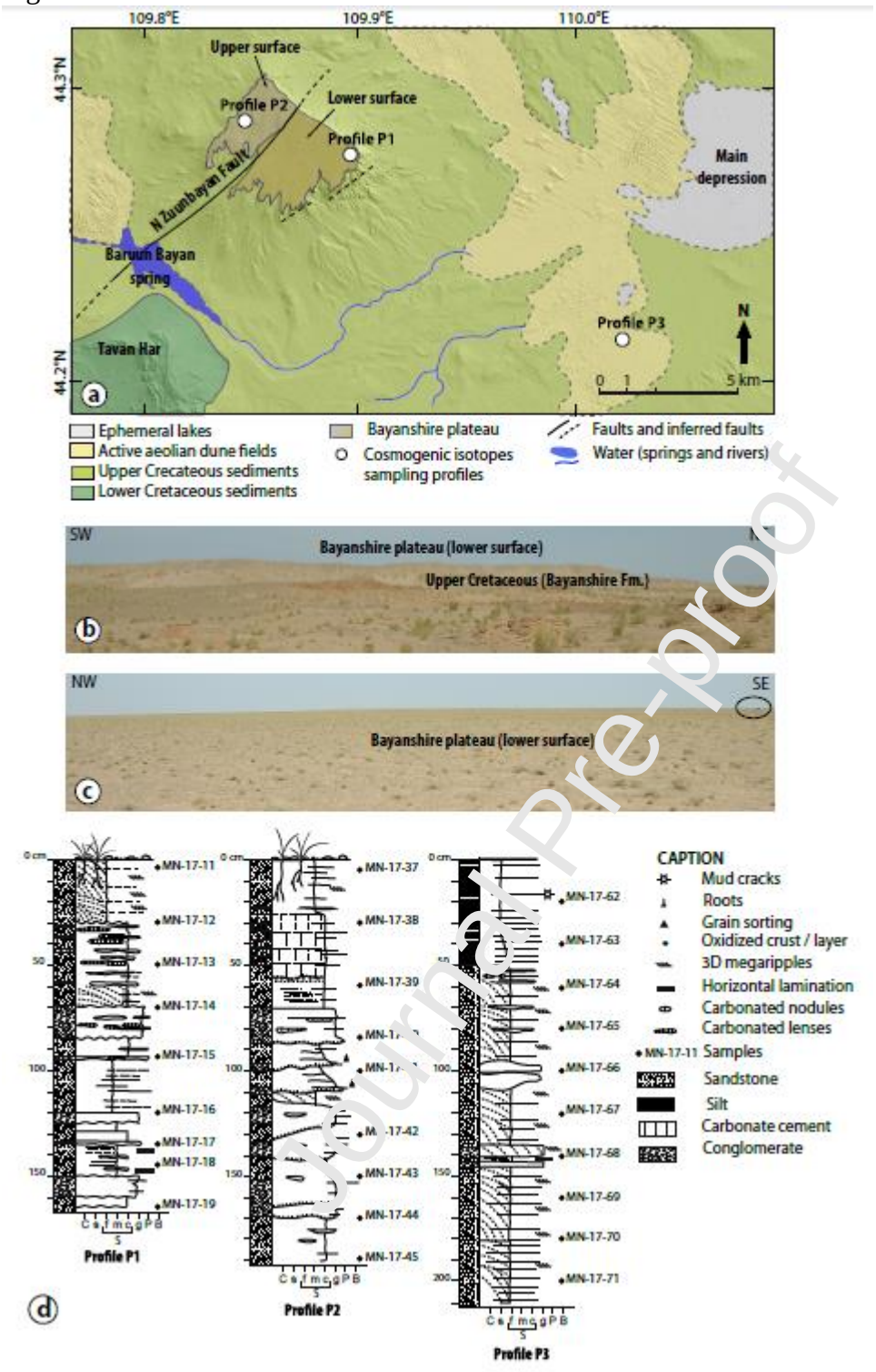

Figure 12

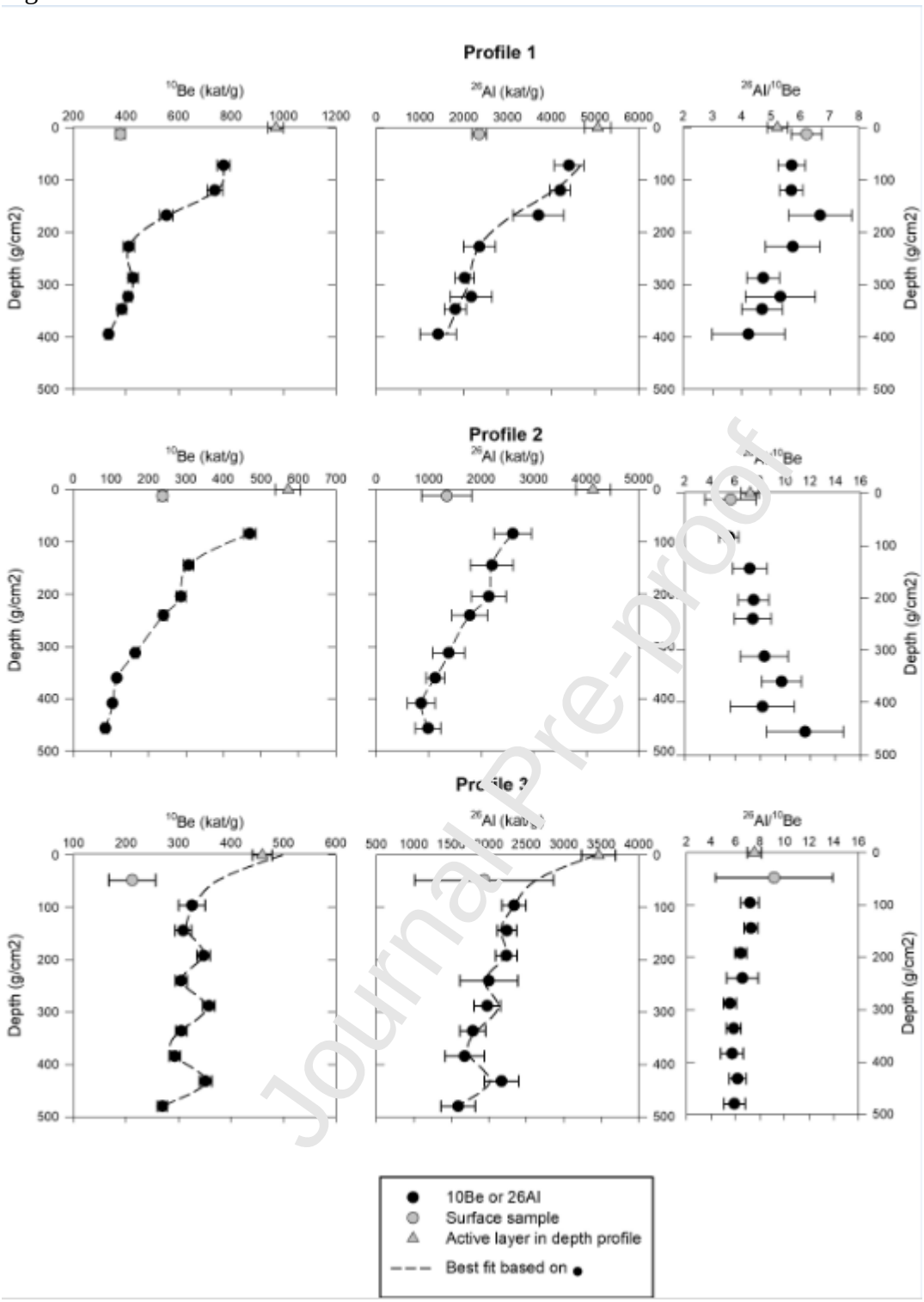

Figure 13

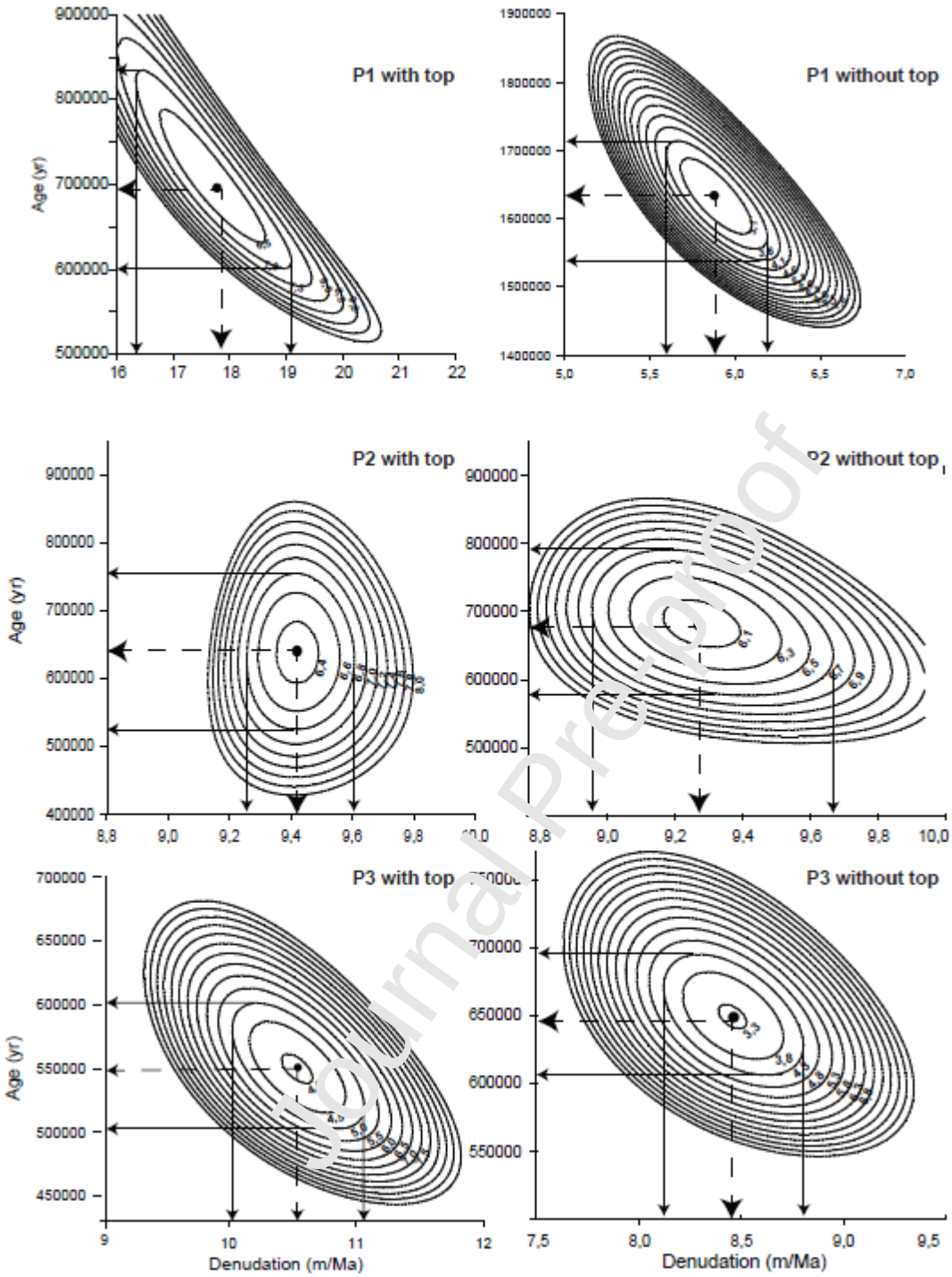

Figure 14

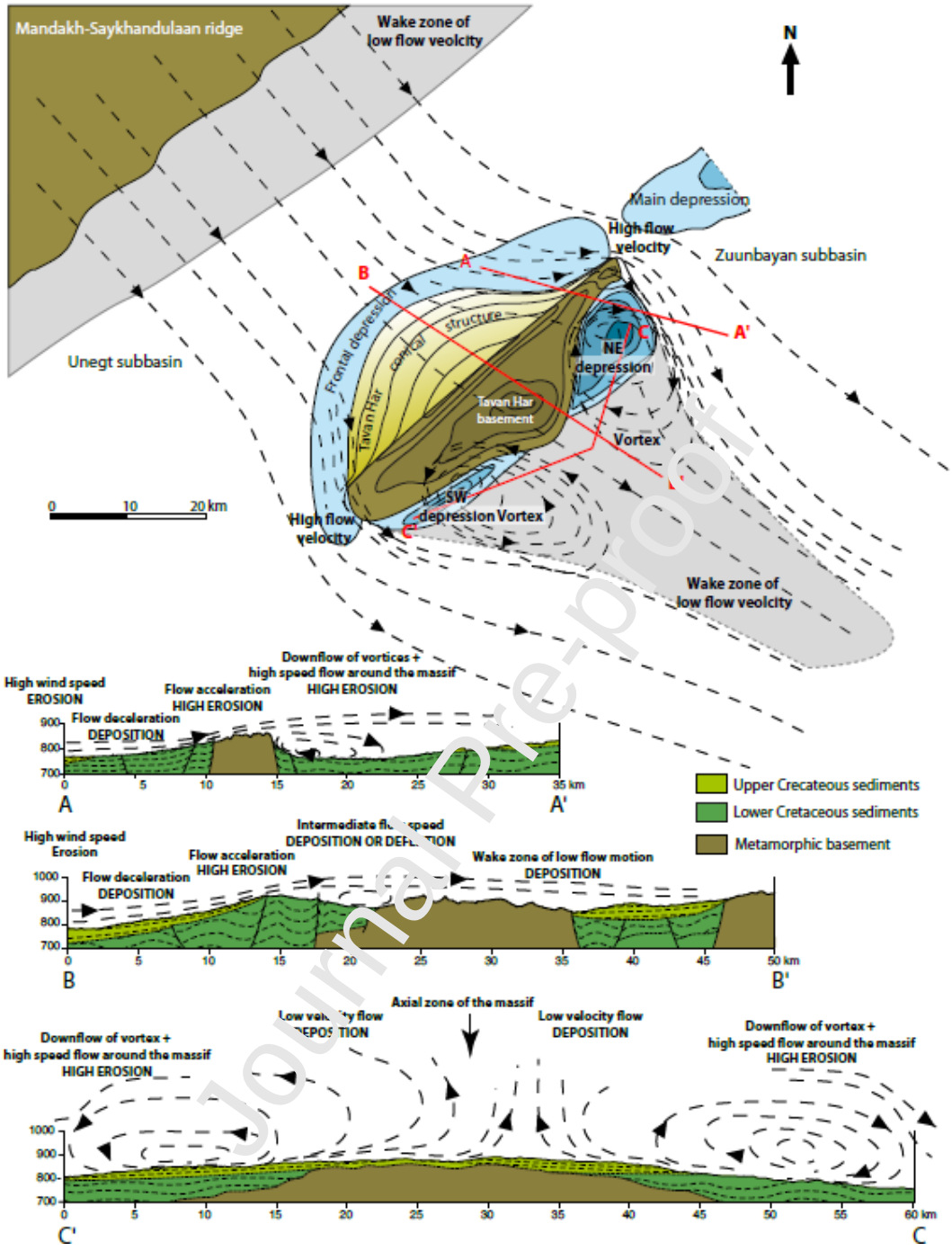
Mandakh-Saykhandulaan ridge
Wake zone of low flow veolcity
N
Main depression
High flow velocity
Zuunbayan subbasin
B
A
A'
Frontal depression
central structure
Tavan Har
Unegt subbasin
NE depression
Tavan Har basement
Vortex
C
C'
0 10 20 km
SW depression Vortex
High flow velocity
Wake zone of low flow veolcity
High wind speed EROSION
Flow deceleration DEPOSITION
Flow acceleration HIGH EROSION
Downflow of vortices + high speed flow around the massif HIGH EROSION
A
A'
Upper Crecateous sediments
Lower Cretaceous sediments
Metamorphic basement
High wind speed Erosion
Flow deceleration DEPOSITION
Flow acceleration HIGH EROSION
Wake zone of low flow motion DEPOSITION
B
B'
Downflow of vortex + high speed flow around the massif HIGH EROSION
Axial zone of the massif
Low velocity flow DEPOSITION
Downflow of vortex + high speed flow around the massif HIGH EROSION
C'
C

Figure 15

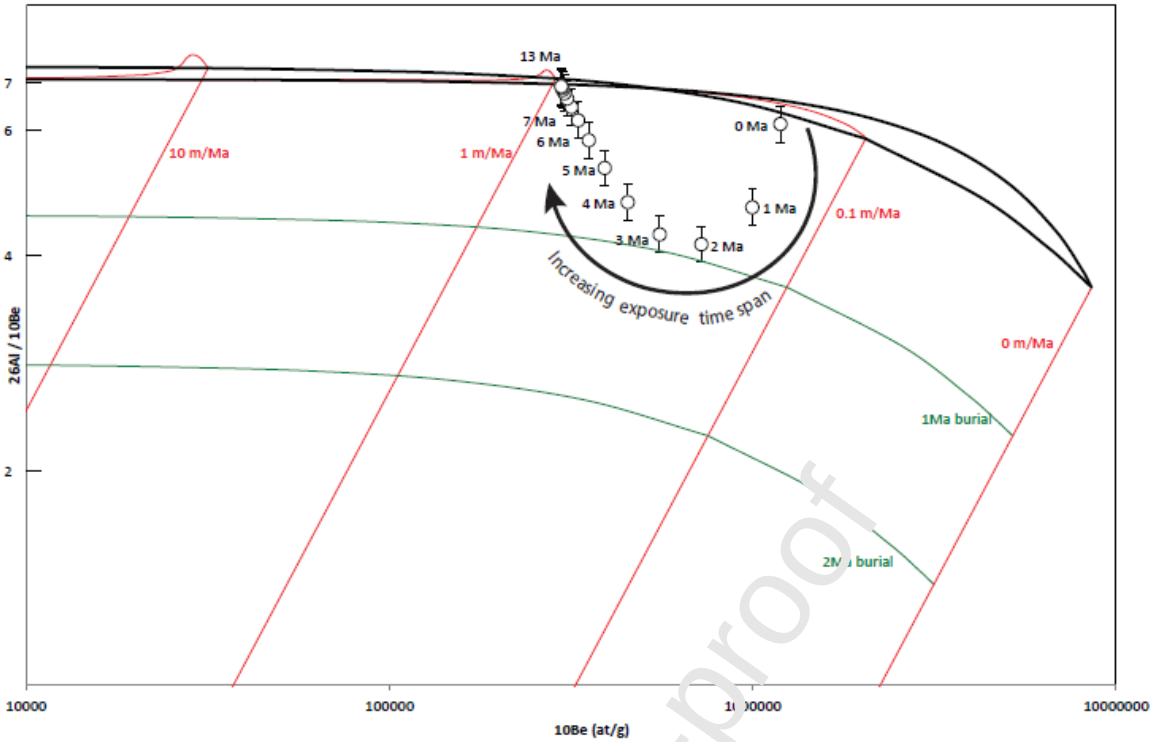

Declaration of interests

X The authors declare that they have no known competing financial interests or personal relationships that could have appeared to influence the work reported in this paper.

☐The authors declare the following financial interests/personal relationships which may be considered as potential competing interests:

Highlights

- Non-erodible obstacles in semi-arid sedimentary basins focus deflation
- Enhanced deflation zones form sub-depocenters controlling local drainage systems
- Fluvial – aeolian interactions are described in a conceptual erosion model
- Cosmogenic 10Be and 26Al analysis indicate generally low erosion rates in Gobi desert
- Erosion rates increased in the Gobi region after the Middle-Pleistocene transition